


RESEARCH ARTICLE

10.1029/2021MS002964

Key Points:

- Overview of Climate Modeling Alliance Land model at the global scale and comparison to existing products
- Vegetation gross primary productivity, transpiration, and hyperspectral canopy radiative transfer are simulated simultaneously
- Modeled fluxes and canopy reflectance and fluorescence well capture the spatial patterns across the globe compared to existing observations

Supporting Information:

Supporting Information may be found in the online version of this article.

Correspondence to:

Y. Wang, A. A. Bloom and C. Frankenberg,
wuyjie@caltech.edu;
alexis.a.bloom@jpl.nasa.gov;
cfranken@caltech.edu

Citation:

Wang, Y., Braghiere, R. K., Longo, M., Norton, A. J., Köhler, P., Doughty, R., et al. (2023). Modeling global vegetation gross primary productivity, transpiration and hyperspectral canopy radiative transfer simultaneously using a next generation land surface model—CliMA Land. *Journal of Advances in Modeling Earth Systems*, 15, e2021MS002964. <https://doi.org/10.1029/2021MS002964>







Received 22 DEC 2021

Accepted 26 FEB 2023

Author Contributions:

Conceptualization: Y. Wang, A. A. Bloom, C. Frankenberg

Modeling Global Vegetation Gross Primary Productivity, Transpiration and Hyperspectral Canopy Radiative Transfer Simultaneously Using a Next Generation Land Surface Model—CliMA Land

Y. Wang¹ , R. K. Braghiere^{1,2} , M. Longo^{2,3}, A. J. Norton², P. Köhler¹, R. Doughty^{1,4} , Y. Yin¹ , A. A. Bloom² , and C. Frankenberg^{1,2} 

¹Division of Geological and Planetary Sciences, California Institute of Technology, Pasadena, CA, USA, ²Jet Propulsion Laboratory, California Institute of Technology, Pasadena, CA, USA, ³Climate and Ecosystem Sciences Division, Lawrence Berkeley National Laboratory, Berkeley, CA, USA, ⁴College of Atmospheric & Geographic Sciences, GeoCarb Mission, University of Oklahoma, Norman, OK, USA

Abstract Recent progress in satellite observations has provided unprecedented opportunities to monitor vegetation activity at global scale. However, a major challenge in fully utilizing remotely sensed data to constrain land surface models (LSMs) lies in inconsistencies between simulated and observed quantities. For example, gross primary productivity (GPP) and transpiration (T) that traditional LSMs simulate are not directly measurable from space, although they can be inferred from spaceborne observations using assumptions that are inconsistent with those LSMs. In comparison, canopy reflectance and fluorescence spectra that satellites can detect are not modeled by traditional LSMs. To bridge these quantities, we presented an overview of the next generation land model developed within the Climate Modeling Alliance (CliMA), and simulated global GPP, T, and hyperspectral canopy radiative transfer (RT; 400–2,500 nm for reflectance, 640–850 nm for fluorescence) at hourly time step and 1° spatial resolution using CliMA Land. CliMA Land predicts vegetation indices and outgoing radiances, including solar-induced chlorophyll fluorescence (SIF), normalized difference vegetation index (NDVI), enhanced vegetation index (EVI), and near infrared reflectance of vegetation (NIRv) for any given sun-sensor geometry. The spatial patterns of modeled GPP, T, SIF, NDVI, EVI, and NIRv correlate significantly with existing data-driven products (mean $R^2 = 0.777$ for 9 products). CliMA Land would be also useful in high temporal resolution simulations, for example, providing insights into when GPP, SIF, and NIRv diverge.

Plain Language Summary Terrestrial plants exchange water for CO₂, but there is not a direct way to measure the carbon gain and water loss at the global scale. Researchers often use eddy covariance flux tower measurements and satellite observations to infer vegetation gross primary productivity (GPP) and transpiration (T). However, flux towers with high temporal resolution are too sparsely distributed, and satellites with high spatial coverage can only detect vegetation properties indirectly, such as solar induced chlorophyll fluorescence, rather than GPP and T themselves. We bridge these two aspects in a new generation land surface model that simultaneously simulates GPP and T, as well as spectrally resolved canopy radiative transfer. We compare our model outputs directly to not only GPP and T estimations but also satellite retrievals of fluorescence and vegetation indices. We show that our new model can represent how GPP and T, as well as canopy radiative properties vary across the globe.

1. Introduction

The land system sequesters approximately 25% of anthropogenic CO₂ emissions (Le Quéré et al., 2018), thus slows the increase of atmospheric CO₂ concentration and global climate change. However, it is highly uncertain how the terrestrial carbon sink strength will change in the future given that warmer global temperatures impact vegetation carbon fixation in diverging ways whereas higher CO₂ concentration leads to higher water use efficiency (Fernández-Martínez et al., 2019; Sperry et al., 2019) and that nutrient limitation modulates vegetation responses to elevated CO₂ (Terrer et al., 2019). Despite the importance of the magnitude of land net CO₂ uptake, overall spatial and temporal patterns of global terrestrial carbon sink strength remain poorly understood given the lack of direct observations at the landscape scale (e.g., in a grid cell) for the entire globe (D. N. Huntzinger

© 2023 The Authors. Journal of Advances in Modeling Earth Systems published by Wiley Periodicals LLC on behalf of American Geophysical Union. This is an open access article under the terms of the [Creative Commons Attribution-NonCommercial License](https://creativecommons.org/licenses/by-nc/4.0/), which permits use, distribution and reproduction in any medium, provided the original work is properly cited and is not used for commercial purposes.

Data curation: Y. Wang, R. K. Braghiere, M. Longo, A. J. Norton, P. Köhler, R. Doughty, A. A. Bloom, C. Frankenberg
Formal analysis: Y. Wang, R. K. Braghiere, M. Longo, A. J. Norton, P. Köhler, R. Doughty, A. A. Bloom, C. Frankenberg
Funding acquisition: C. Frankenberg
Investigation: Y. Wang, R. K. Braghiere, M. Longo, A. J. Norton, P. Köhler, R. Doughty, A. A. Bloom, C. Frankenberg
Methodology: Y. Wang, R. K. Braghiere, P. Köhler, C. Frankenberg
Project Administration: A. A. Bloom, C. Frankenberg
Resources: Y. Wang, R. K. Braghiere, M. Longo, A. J. Norton, P. Köhler, R. Doughty, A. A. Bloom, C. Frankenberg
Software: Y. Wang, C. Frankenberg
Supervision: C. Frankenberg
Validation: Y. Wang, R. K. Braghiere, C. Frankenberg
Visualization: Y. Wang
Writing – original draft: Y. Wang, R. K. Braghiere, M. Longo, A. J. Norton, P. Köhler, R. Doughty, A. A. Bloom, C. Frankenberg
Writing – review & editing: Y. Wang, R. K. Braghiere, M. Longo, A. J. Norton, P. Köhler, R. Doughty, A. A. Bloom, C. Frankenberg

et al., 2013; Wei et al., 2014; Sitch et al., 2015). As a result, the estimation of the global terrestrial carbon sink is largely dependent on data interpolation and/or modeling (O'Neill et al., 2016; Taylor et al., 2012).

Net ecosystem exchange (NEE) is the difference between gross primary productivity (GPP) and total ecosystem respiration (TER): $NEE = GPP - TER$. Since TER cannot be directly or indirectly quantified through remote sensing observations, research has been focused on correlating the observations to GPP rather than NEE. However, global scale GPP products (both data-driven and modeled products) from various studies differ dramatically (Anav et al., 2015; Zhang & Ye, 2021) due to differences in (a) the module choice from various parameterization schemes, such as stomatal model (Medlyn, Duursma, & Zeppel, 2011), soil moisture response (Powell et al., 2013; Trugman et al., 2018), and canopy structure (Braghiere et al., 2019, 2020; Li et al., 2022), and (b) the major drivers used to force the model for data-driven products and meteorological forcing and vegetation maps for land surface model (LSM) simulations (D. Huntzinger et al., 2021), such as flux tower data (e.g., Jung et al., 2011; Jung et al., 2020; Tramontana et al., 2016) or remote sensing data (e.g., Zhang et al., 2017). Furthermore, the rapidly changing climate and increasing atmospheric CO₂ make it more challenging for the models to agree (Anav et al., 2013, 2015; Arora et al., 2013; Jones et al., 2013; Zhang & Ye, 2021).

GPP difference caused by module choice may be considered as a result of the various forms of forcing data. For example, eddy covariance flux towers provide relatively high quality half-hourly carbon and water fluxes (Baldocchi, 2020; Baldocchi et al., 2001), but are too sparsely distributed; and modelers have to rely on data interpolation for global interpretation. Also, GPP is not directly measured but partitioned from NEE using nighttime values to proxy TER, and this partitioning could result in biased GPP estimates (Wehr et al., 2016). In comparison, spaceborne remote sensing data provide high spatial coverage (Schimel et al., 2015, 2019), but often have coarse temporal resolution and cannot directly measure carbon or water flux. Statistical models that attempt to quantify GPP from remote sensing data often have to rely on empirically correlating GPP with various quantities based on reflectance and/or fluorescence (e.g., Gentemann et al., 2020; Jung et al., 2020; Turner et al., 2006). As a result, a satisfactory approach to set up LSMs consistently at the global scale is lacking, and model-observation comparisons are inconsistent. In theory, if the LSMs can correctly parameterize the vegetation processes and are calibrated using the same high quality flux and meteorological forcing data, these models should be able to predict similar GPP once their model parameters (e.g., leaf area index, plant functional type distributions, leaf photosynthetic capacity, and plant hydraulic traits) are optimized for the input data. Currently, high quality carbon and water flux data are sparse, which makes model calibration and development challenging. Therefore, a key step for improving land modeling is to (a) equip LSMs with features to simulate observations corresponding to multiple data sources and (b) calibrate the LSMs by minimizing the model-data mismatch.

Remotely sensed data that are useful to constrain vegetation carbon and water fluxes at regional and global scales are mostly based on observed reflected radiances, emitted radiances, and optical depths of vegetation canopies (e.g., Badgley et al., 2017; Konings et al., 2021; Sun et al., 2017). Among the various index and radiance measures, solar-induced chlorophyll fluorescence (SIF) and near infrared reflectance of vegetation (NIRv) are promising candidates for estimating GPP given their overall good correlations with GPP (Badgley et al., 2017, 2019; Dechant et al., 2022; Doughty et al., 2021; Frankenberg et al., 2011; Sun et al., 2018; Wu et al., 2020). Nevertheless, the intermediate step of translating SIF and/or NIRv to GPP may introduce additional biases given the decoupled correlations among them in light saturated environments (Zhang et al., 2016), drought stressed conditions (Helm et al., 2020), cold winters (Magney et al., 2019), and over diversely structured vegetation (Braghiere et al., 2021).

Alternatively, a better way to utilize the remote sensing data would be to match modeled canopy fluorescence and reflectance at specific wavelengths/bands and even the entire spectra to satellite retrievals directly (Norton et al., 2018; Shiklomanov et al., 2021). This, however, requires LSMs to move from simple broadband canopy radiative transfer (RT) to a hyperspectral canopy RT in order to utilize spectrally resolved remote sensing data, which most existing LSMs are not designed to do. To better benchmark, optimize, and improve the LSMs, researchers have adapted LSMs to incorporate various SIF formulations, most of which were based on the Soil Canopy Observation of Photosynthesis and Energy fluxes model (SCOPE; van der Tol et al., 2009; Parazoo et al., 2020). These SIF implementations can be categorized to (a) online simulation through bridging LSM and SCOPE (Koffi et al., 2015; Norton et al., 2018, 2019) and (b) offline simulation via add-on SIF models or emulators (RT for SIF differs from that for photosynthesis) (Bacour et al., 2019; Lee et al., 2015; Qiu et al., 2019; Raczka et al., 2019). However, the latter approach discards useful information that hyperspectral and multi-layer

RT scheme contains, such as the sun-sensor geometry and vertical profiles of fluorescence and photosynthesis yields, which interact non-linearly.

Our recent efforts bridge land modeling and remote sensing observations together in a new LSM as part of a new generation Earth system model within the Climate Modeling Alliance (CliMA) (Y. Wang et al., 2021). The new model (CliMA Land) can simulate hyperspectral canopy RT in a multi-layer canopy, enabling us to simultaneously simulate canopy GPP and transpiration (T) as well as corresponding canopy fluorescence and reflectance spectra. CliMA Land improves SIF representation at the canopy scale by accounting for canopy clumping index (Braghiere et al., 2021) and well captures the ecosystem net carbon and water fluxes measured at flux tower sites (Y. Wang et al., 2021). In particular, the simultaneously simulated GPP, SIF, and NIRv allow for many potential studies that were not possible, say the diurnal cycles and correlations among SIF, NIRv, and GPP at various temporal resolutions.

In this study, we (a) describe the general model framework of CliMA Land, (b) detail the model setup and simulation procedure, and (c) show our first global run at hourly time step and 1° resolution using CliMA Land. In Section 3, we investigate how well CliMA Land captures the spatial patterns of GPP, T, SIF, and other vegetation indices. Finally, we discuss potential ways to improve the predictive skills of CliMA Land.

2. Materials and Methods

2.1. CliMA Land Overview

CliMA Land is coded in Julia, a dynamically typed programming language that feels like scripting language (Bezanson et al., 2017), and is easier for users to read and modify compared to programming languages such as Fortran used in most existing LSMs. The major principle of CliMA Land model design is modularity, for example, each component/module of CliMA Land can be used as a stand alone package. We further separate the core functions (functions that parameterize the processes) from configuration functions (functions that operate model parameters) to allow for users' customization over the parameters; and one can choose whether, when, and how to operate the parameters using either in-built or external functions. See Table 1 for the summary of how CliMA Land differs from traditional LSMs in its code design and scientific merits. CliMA Land code and documentation are publicly and freely available at <https://github.com/CliMA/Land> (examples provided). For the present study, we used the soil-plant-air continuum (SPAC) module of CliMA Land to run global simulations of canopy carbon and water fluxes as well as canopy optical properties. The exact version of the model and code to run global simulations (model tag A6) are archived at Zenodo (Y. Wang, 2023a).

The SPAC module of CliMA Land (v0.1) consists of four sub-modules: plant hydraulics, photosynthesis, stomatal models, and canopy RT (see Figure 1 for the SPAC module hierarchy). We implement a number of alternative parameterization schemes in each sub-module, and users are free to customize the model setup (select appropriate schemes) and configuration (configure model parameters) for research at different scales (for instance, one can use canopy RT sub-module to simulate canopy light environment without invoking other sub-modules). We note that CliMA Land is a model based on plant traits, and the difference among sites or grid cells is represented by the changes in traits (such as photosynthetic capacity and hydraulic conductivity) rather than plant functional types. See Section 2.2 and Table 3 for more details of how the traits are implemented and used in CliMA Land.

To date, the SPAC module of CliMA Land has been tested in the following studies: (a) simulating carbon and water fluxes as well as SIF with sun-sensor geometry of overpass satellite at two flux tower sites using three stomatal models and a multi-layer hyperspectral canopy RT scheme (Y. Wang et al., 2021), (b) implementing clumping index to improve SIF simulation (Braghiere et al., 2021), and (c) evaluating how canopy complexity impacts canopy carbon, water, and SIF fluxes (Y. Wang & Frankenberg, 2022a). In the present study, we utilized these tested functionalities of the CliMA Land to assess how well the model performs at the global scale, regarding its simulated GPP and T as well as canopy optical properties.

2.1.1. Plant Hydraulics

Plant hydraulics sub-module in CliMA Land is based on the hydraulic model developed by Sperry and Love (2015) and Sperry et al. (2016). The sub-module partitions a plant into root, stem, and leaf organs, and a specific xylem vulnerability curve is used for each organ (the curve is allowed to differ within and among organs). The organs can be aligned in a flexible way. For example, a tree comprises a multi-layer root system, a trunk (stem), a

Table 1

Summary of How Climate Modeling Alliance (CliMA) Land Differ From Traditional Land Surface Models

Traditional land surface model	CliMA land
Code design	
Core functions and model configuration are often hard coded, and it is not convenient to switch the setups and calculations during a simulation	Core and configuration functions are separated (e.g., model parameters and intermediate variables can be accessed and modified) so that users can freely adjust the parameters and calculations through built-in and/or external functions at each time step
Code usually cannot be used directly in research that operates at smaller scales, for example, leaf level	Code is highly modularized, and each sub-module can be used as a standalone package for research and other models with minimum efforts
Typically written in Fortran, and thus has a steep learning curve for beginners	Written in Julia, a modern script-like language, has shallow learning curve, and is friendly to read and use for beginners
Users cannot redefine hard coded parameters and functions	Users can multiple dispatch functions (e.g., same function name for different functionality) and overwrite imported parameters and functions
Users are given limited parameterization schemes, and cannot replace those with externally defined schemes	More complex embedded model schemes are provided for users to choose from, and users can also expand the model with new parameterization schemes (enabled by Julia abstract type feature)
Scientific merits	
Not designed to run hyperspectral radiative transfer scheme, so that cannot use remote sensing data directly (such as reflectance and fluorescence at a given sun-sensor geometry)	Equipped to run hyperspectral canopy radiative transfer, ready for utilizing remote sensing data from 400 to 2,500 nm with the given sun-sensor geometry
Model parameters are often plant function type (PFT) based, and thus have limited capability to handle site-to-site variations (for example, all broad-leaf deciduous forests have the same leaf absorption features)	Model parameters are not PFT based but plant trait based, and globally gridded data sets can be readily used to account for site-to-site spatial and temporal variations
Photosynthesis module is limited to classic C3 and C4 models that only compute photosynthetic rates	More recent updates on photosynthesis and fluorescence models have been implemented, and the photosynthesis module can compute leaf level fluorescence parameters at the same time
Plant hydraulic system is often represented as one or a few xylem element(s), and has limited capability to handle drought legacy, capacitance, and flow/pressure profiles	Plant hydraulic system can be customized to different complexities; is capable of handling drought legacy, water storage, flow/pressure profiles, temperature dependency, and soil water redistribution; and works seamlessly with statistical and optimality-based stomatal models
Stomatal models are statistical models, and plant traits do not impact the model parameters	Besides the statistical stomatal models, a number of optimality based stomatal models have been implemented to better bridge plant traits and physiology to the model

multi-layer canopy system (stem and leaf in series in each layer); a grass comprises a multi-layer root system and a multi-layer canopy system (only leaf is present in each layer). Further, the plant hydraulics sub-module allows for customizing root and stem height change, and thus is able to account for a gravitational pressure drop in the xylem. Moreover, there is a drought legacy variable in each hydraulic organ (the xylem remembers the minimal xylem pressure and thus minimal hydraulic conductance it has experienced, and xylem hydraulic conductance is not allowed to be higher than this memory conductance due to irreversible xylem cavitation), and addressing this gives more realistic stomatal response to the environment after a drought (W. R. L. Anderegg et al., 2015; Y. Wang et al., 2020). We also account for temperature effects on water viscosity and surface tension in our plant hydraulics module, which could otherwise result in non-negligible simulated water transport biases (e.g., 1°C difference in water temperature potentially results in c. 2.4% change in maximum hydraulic conductance; Reid et al., 1987; Y. Wang & Frankenberg, 2022b).

Plant hydraulic architecture may impact the stomatal models in CliMA Land (not always as some stomatal models do not rely on plant hydraulics at all, see examples in Section 2.1.3). With the ascent of sap along the xylem, xylem water pressure typically gets more and more negative, potentially resulting in xylem cavitation. The higher the water flux in the xylem and/or the drier the soil, the higher the risk of xylem cavitation. Loss of plant water transport capability may harm plants' leaf gas exchange performance given the limited water supply to leaves, and thus plants may regulate their stomata to alleviate the risk (Sperry & Love, 2015). Combining photosynthetic carbon gain and hydraulic risk leads to a variety of stomatal optimization models that simulate stomatal behavior using plant traits rather than empirically fitted parameters (see Y. Wang et al. (2020) for an

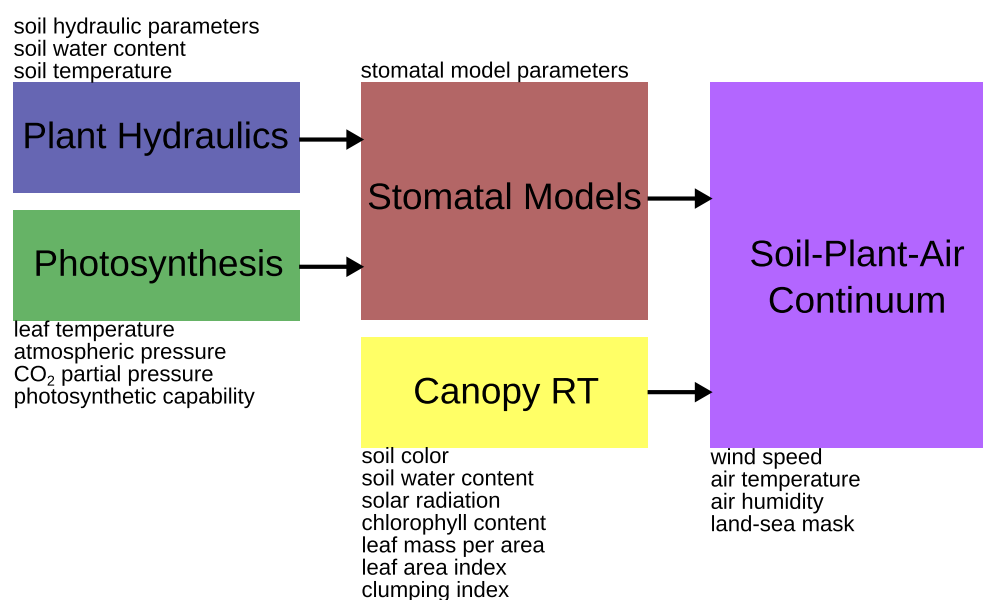


Figure 1. Model hierarchy of soil-plant-air continuum (SPAC) module of Climate Modeling Alliance (CliMA) Land. CliMA Land SPAC module consists of four key sub-modules: plant hydraulics, photosynthesis, stomatal models, and canopy radiative transfer (RT). Plant hydraulic module accounts for the water movement from soil to air; photosynthesis module computes the leaf level gas exchange rates; stomatal models module is responsible for decision making about how plants regulate the stomatal opening; and canopy RT module simulates the canopy light environment and optical properties such as reflectance and fluorescence spectra. SPAC module is responsible for coordinating the sequences of function calls. For example, at any time step, SPAC calls (a) canopy RT module to run shortwave radiation and sync the radiation information to leaves at different canopy layers; (b) Photosynthesis, PlantHydraulics, and StomataModels to compute stomatal conductance; (c) compute the leaf level fluorescence quantum yield, and sync it to Canopy RT; and (d) compute fluorescence at the viewer's direction. Black arrows indicate the dependencies within the SPAC module, for example, the photosynthesis and plant hydraulics sub-modules are direct dependencies of the stomatal models sub-module. The text next to each color box describes the parameters and weather drivers used by CliMA Land in the present study.

overview). Furthermore, plant hydraulic status is also used in more and more empirical stomatal models (e.g., Kennedy et al., 2019), acting as a tuning factor to link stomatal responses to soil moisture status. We note that due to the limited knowledge of global plant hydraulic trait maps, we were not able to run CliMA Land using plant hydraulics-based stomatal models; thus we used the stomatal model develop by Medlyn, Duursma, Eamus, et al. (2011) combined with a tuning factor based on soil water moisture in the present study.

2.1.2. Photosynthesis

Photosynthesis sub-module supports three photosynthesis models, including a C3 model based on Farquhar et al. (1980), a C4 model based on Collatz et al. (1992), and a new C3 model based on Cytochrome activity developed by Johnson and Berry (2021). To compute the photosystem level fluorescence quantum yield (photosystem I and photosystem II combined), the two classic photosynthesis models can be used along with the fluorescence model in van der Tol et al. (2014). The Cytochrome-based C3 photosynthesis model includes photosystem level fluorescence quantum yield calculations (separately for photosystem I and photosystem II) (Johnson & Berry, 2021). Due to the lack of global maps of C3 Cytochrome photosynthesis model parameters, we used the classic photosynthesis models in the present study. For the fluorescence model, we used the parameters derived for measurements from drought experiments ($K_N^o = 5.01$, $\alpha = 1.93$, and $\beta = 10$ as in their Equation 19; van der Tol et al., 2014).

2.1.3. Stomatal Control

Stomatal behavior in CliMA Land can be simulated using either empirical models that rely on statistically fitted parameters or stomatal optimization models that are based on plant traits and processes (Table 2). The empirical models can be used along with two general types of tuning factors to force stomatal response to drought, one of which takes effect through tuning the empirical equation parameters (such as the slope parameter g_1) and another takes effect via down-regulating photosynthetic capacity (e.g., Kennedy et al., 2019). The optimality

Table 2
Stomatal Models Supported by Climate Modeling Alliance Land

Type	Model	Formulation	β
Empirical	Ball et al. (1987)	$g_s = g_0 + \beta \cdot g_1 \cdot RH \cdot \frac{A}{C_s}$	g_1
		$g_s = g_0 + g_1 \cdot RH \cdot \frac{A(\beta)}{C_s}$	V_{cmax}
	Leuning (1995)	$g_s = g_0 + \beta \cdot g_1 \cdot \frac{A}{C_s - \Gamma^*} \cdot \frac{d_0}{d_0 + VPD}$	g_1
		$g_s = g_0 + g_1 \cdot \frac{A(\beta)}{C_s - \Gamma^*} \cdot \frac{d_0}{d_0 + VPD}$	V_{cmax}
Optimality	Medlyn, Duursma, Eamus, et al. (2011)	$g_s = g_0 + \beta \cdot 1.6 \cdot \frac{A}{C_a} \cdot \left(1 + \frac{g_1}{\sqrt{VPD}}\right)$	g_1
		$g_s = g_0 + 1.6 \cdot \frac{A(\beta)}{C_a} \cdot \left(1 + \frac{g_1}{\sqrt{VPD}}\right)$	V_{cmax}
	Sperry et al. (2017)	$\frac{\partial A}{\partial E} = \frac{\partial \Theta}{\partial E} = -\frac{\partial K}{\partial E} \cdot \frac{A_{max}}{K_{max}}$	
	Eller et al. (2018)	$\frac{\partial A}{\partial E} = \frac{\partial \Theta}{\partial E} = -\frac{\partial K}{\partial E} \cdot \frac{A}{K}$	
	W. R. Anderegg et al. (2018)	$\frac{\partial A}{\partial E} = \frac{\partial \Theta}{\partial E} = \frac{2 \cdot a \cdot P + b}{K}$	
	Y. Wang et al. (2020)	$\frac{\partial A}{\partial E} = \frac{\partial \Theta}{\partial E} = \frac{A}{E_{crit} - E}$	

Note. The empirical models compute stomatal conductance (g_s) through statistical formulations, whereas the optimality based models compute g_s through finding the leaf transpiration rate where photosynthetic rate (A) and risk (Θ) are optimized. g_0 , g_1 , and d_0 : empirical equation parameters; β : soil moisture tuning factor; RH: relative humidity; C_s : atmospheric CO₂ concentration; C_s : leaf surface CO₂ concentration; Γ^* : CO₂ compensation point with the absence of respiration; VPD: vapor pressure deficit; a and b : W. R. Anderegg et al. (2018) equation parameters; P : leaf xylem water pressure; E : leaf transpiration rate; E_{crit} : critical leaf transpiration rate beyond which leaf desiccates; K : $\partial E / \partial P$; A_{max} : maximum photosynthetic rate at given soil moisture setting; K_{max} : maximum K when $E = 0$; V_{cmax} : maximum carboxylation rate at a reference temperature of 25°C.

based models are less dependent on fitting parameters and performed well compared to empirical models, though the traits required to run the models are more difficult to obtain (W. R. Anderegg et al., 2018; Sabot et al., 2022; Venturas et al., 2018; Y. Wang et al., 2020).

As a result, empirical models are still the top candidates for LSMs before reliable spatially resolved plant hydraulics trait maps become available. Similarly, using a tuning factor (also known as beta function; Powell et al. (2013)) on empirical equation parameter g_1 or photosynthetic capacity based on plant hydraulics at the global scale does not work either. For example, Kennedy et al. (2019) proposed to use hydraulic conductance to tune leaf photosynthetic capacity; however, the calculation of hydraulic conductance relies on the xylem vulnerability curve as well as whole plant hydraulic conductance, which are spatially unknown at global scales at present. Thus, to date, simulating global land carbon and water fluxes is still limited to empirical models and tuning factors based on soil conditions rather than plant hydraulics. In the present study, we used (Medlyn, Duursma, Eamus, et al., 2011) model along with a tuning factor based on g_1 , and stomatal conductance (g_s) is computed from

$$g_s = g_0 + \beta \cdot 1.6 \cdot \frac{A}{C_a} \cdot \left(1 + \frac{g_1}{\sqrt{VPD}}\right), \quad (1)$$

where A is net photosynthetic rate, C_a is atmospheric CO₂ concentration, vapor pressure deficit (VPD) is leaf to air vapor pressure deficit, and β is a linear tuning factor based soil water potential:

$$\beta = \max \left[0, \min \left(1, \frac{p_{soil} - p_{min}}{p_{max} - p_{min}} \right) \right], \quad (2)$$

where p_{max} and p_{min} are parameters describing the linear tuning factor ($p_{max} = 0$ MPa, and $p_{min} = -5$ MPa by default).

2.1.4. Canopy Radiative Transfer

CLiMA Land features two canopy RT schemes: single layered two leaf RT scheme with sunlit and shaded fractions simulating broadband reflectance and transmittance (Campbell & Norman, 1998), and a vertically layered canopy RT scheme with leaf angular distribution simulating hyperspectral reflectance and transmittance (adapted

Table 3
Global Scale Data Sets Used in the Present Study

Variable	Resolution	Reference
Soil Parameters		
Inverse of air entry value	120X	Dai et al. (2019) ^a
Soil pore-size distribution	120X	Dai et al. (2019) ^a
Residual soil water content	120X	Dai et al. (2019) ^a
Saturated soil water content	120X	Dai et al. (2019) ^a
Soil color classification	2X	Lawrence and Chase (2007)
Meteorological Drivers		
Wind speed at 10 m	4X, 1H	Hersbach et al. (2018)
Dew point temperature at 2 m	4X, 1H	Hersbach et al. (2018)
Air temperature at 2 m	4X, 1H	Hersbach et al. (2018)
Skin temperature	4X, 1H	Hersbach et al. (2018)
Mean direct surface shortwave radiation	4X, 1H	Hersbach et al. (2018)
Mean total surface shortwave radiation	4X, 1H	Hersbach et al. (2018)
Surface atmospheric pressure	4X, 1H	Hersbach et al. (2018)
Soil temperature	4X, 1H	Hersbach et al. (2018) ^b
Soil volumetric water content	4X, 1H	Hersbach et al. (2018) ^b
Percentage of land in a grid cell	4X	Hersbach et al. (2018)
Annual mean CO ₂ concentration		https://gml.noaa.gov/ccgg/trends
Plant traits		
Leaf chlorophyll content	2X, 7D	Croft et al. (2020) ^c
Leaf mass per area	2X	Butler et al. (2017)
Leaf photosynthetic capacity	2X	Luo et al. (2021) ^d
Stomatal model g_1	2X	De Kauwe et al. (2015) ^e
Leaf area index	2X, 8D	Yuan et al. (2011)
Clumping index	240X	He et al. (2012)

Note. In column “Resolution,” NX means the spatial resolution is $1/N^\circ$, and MT stands for the temporal resolution (M is an number, T is a string for time: H for hour and D for day; e.g., 1H means 1 hr and 7D means 7 days).

^aThese parameters describe the soil retention curve using van Genuchten (1980) equation. The data sets include parameters for 4 soil layers, with the boundary depth from 0 to 0.1, 0.35, 1, and 3 m. We partitioned plant root layering accordingly to these 4 layers. ^bSoil layering of ERA5 differs slightly from the soil hydraulic parameters (Dai et al., 2019) in that the boundary depths are 0–0.07, 0.28, 1, and 2.89 m. We used the soil temperature and water content for each soil layer despite the minor mismatch in soil depth profiles. ^cLeaf carotenoid content is assumed to be 1/7 of leaf chlorophyll content. The weekly mean chlorophyll content was averaged from values in the same week from multiple years (2003–2011), and the same leaf chlorophyll content data set was used for simulations at different years. ^dThe maximum carboxylation rate at 25°C ($V_{\text{cmax}25}$) was assumed time-invariant. Maximum electron transport rate at a reference temperature of 25°C— $J_{\text{max}25}$ and respiration rate at a reference temperature of 25°C— $R_{\text{d}25}$ were scaled from $V_{\text{cmax}25}$ in that $J_{\text{max}25} = 1.67 \cdot V_{\text{cmax}25}$ and $R_{\text{d}25} = 0.015 \cdot V_{\text{cmax}25}$, consistent with Sperry et al. (2017). We assumed constant $J_{\text{max}25} : V_{\text{cmax}25}$ and $R_{\text{d}25} : V_{\text{cmax}25}$ ratios due to the lack of global data sets, however we note that there is evidence that they vary across the globe (e.g., Norby et al., 2017; Walker et al., 2014). ^eWe used the community land model plant functional type (PFT) distribution map gridded at $1/2^\circ$ (Lawrence & Chase, 2007) to derive the empirical parameter g_1 at each grid cell. For each grid cell, we calculated the weighted g_1 based on the PFT distribution, and used a $g_0 = 0.001 \text{ mol m}^{-2} \text{ s}^{-1}$.

from SCOPE; van der Tol et al., 2009; Yang et al., 2017). While the inclusion of the two leaf RT scheme allows for compatibility with other land surface or vegetation models that use the same canopy RT scheme, the use of a complex multi-layer canopy RT scheme enables the simulation of canopy reflectance and fluorescence spectra as well as vegetation GPP and T simultaneously, promoting the integration of land modeling with remote sensing observations (Y. Wang et al., 2021). The multi-layered RT scheme in CliMA Land simulates the hyperspectral RT in the wavelength window of 400–2,500 nm, and allows for flexible customization of number of canopy layers,

leaf angular distribution, canopy clumping, and wavelength bins. Moreover, the multi-layer canopy RT scheme also supports vertically resolved heterogeneous micro-climates and leaf physiology within the canopy (Bonan et al., 2018, 2021).

For the hyperspectral multi-layered RT scheme, compared to the original SCOPE canopy RT scheme, (a) we implemented a clumping index to account for the horizontal heterogeneity in the canopy (Braghiere et al., 2019, 2020; Pinty et al., 2006). The inclusion of a clumping index can promote light scattering into lower canopy layers, and improves model predictive skills against benchmark 3D data sets (Braghiere et al., 2021). (b) Compared to the original leaf-level PROSPECT-D model used in SCOPE (F  ret et al., 2017), we accounted for carotenoid absorption as absorbed photosynthetically active radiation (PAR) by the antenna systems, thus photosynthesis and chlorophyll fluorescence (Y. Wang et al., 2021). (c) For each wavelength in the simulated SIF spectrum (400–750 nm for SIF excitation, 640–850 nm for SIF emission), we converted energy flux to photon flux at the excitation stage and computed SIF in terms of photon (to use with fluorescence quantum yield); and then we convert SIF photon flux back to energy flux at the emission stage and compute SIF RT (Y. Wang & Frankenberg, 2022a), thus ensuring conservation of energy considering fluorescence photons are re-emitted at longer wavelengths. (d) We further expand the soil albedo implementation to hyperspectral simulations to make land modeling more realistic in terms of canopy RT and gas exchange simulations (see Text S1 in Supporting Information S1 for more details).

To better compare the model simulations to remote sensing data in the shortwave range (400–2,500 nm), we used the multi-layered hyperspectral RT scheme along with a hyperspectral soil albedo representation in the present study. Through simulating hyperspectral canopy RT and scaling leaf-level gas exchange, we can integrate total GPP and T, and simulate a number of remotely sensible quantities (such as SIF and NIRv) simultaneously at hourly time steps per 1  grid at the global scale. We note that CliMA Land is capable of simulating canopy reflectance and radiance as well as fluorescence at any given sun-sensor geometry (e.g., Figure 16 of Y. Wang et al. (2021)). In the present study, we modeled the canopy optical properties at the nadir direction at every time step, and compared them to the indices derived from bidirectional reflectance distribution function corrected Moderate Resolution Imaging Spectroradiometer (MODIS) data (MCD43A4; (Schaaf & Wang, 2015)) and day length corrected SIF (K  hler et al., 2018, 2020).

2.2. Model Configuration and Simulation

In CliMA Land, we separate the core functions from model parameter configuration, and thus allow for running CliMA Land with various combinations of traits and meteorological drivers. For example, leaf photosynthetic capacity value and its seasonality can be configured from external inputs rather than being hard coded; and users can freely customize these model parameters at each time step. In the present study, we treated a grid cell as a “mono-species” stand in which all plants have the same bulk properties. Table 3 summarizes the global scale data sets we used to configure CliMA Land and drive model simulations in the presented study (corresponding to “gm1” in our model simulations; see Figure 1 for where these parameters and variables were used). The global maps used can be accessed through GriddingMachine (<https://github.com/CliMA/GriddingMachine.jl>), a database and software we developed to distribute globally gridded data sets (Y. Wang et al., 2022).

Note that leaf water content and leaf angular distribution also have great impact on canopy RT simulations. However, given the limited knowledge of how plant hydraulic traits and leaf angular distributions change at the global scale, we used constant equivalent leaf water thickness of 0.09 mm and uniform leaf angular distribution in the present study.

We ran CliMA Land globally at 1  spatial resolution and hourly temporal resolution (because the ERA5 meteorological forcing data is hourly). We regridded the input parameters and variables listed in Table 3 spatially to 1  by averaging all the data that fell into the target grid cell. For each pixel, we performed the annual simulation if (a) none of the input data was missing and (b) the pixel was vegetated. A total of 11,288 grid cells were identified after applying these filtering criteria. Given that it is our first global scale evaluation of CliMA Land, we ran the global simulation (a) by prescribing canopy temperature and soil moisture using ERA5 skin temperature and soil water content, and (b) at relatively coarse spatial resolution to provide an overview of what can be simulated by CliMA Land. Our global simulations for the year 2010 and 2019 with the simulation tag “a6_gm1_wd1” can be found at Y. Wang (2023b).

We ran CliMA Land at steady state mode by iterating the SPAC functions to find the solution at the given environmental conditions (Y. Wang et al., 2021). In brief, at each time step, we (a) calculated soil water potential and

leaf temperature from prescribed ERA5 data, (b) computed the solar zenith angle based on latitude and local time, (c) simulated shortwave RT in the canopy and update the light environment for each canopy layer, (d) updated environmental conditions and leaf temperature per canopy layer, (e) computed steady state stomatal conductance for each leaf angel in each canopy layer by iterating the SPAC functions, (f) modeled leaf level fluorescence quantum yield and computed canopy level optical properties including SIF at nadir viewing direction, and (g) saved the model predicted hourly GPP, T, SIF at 683/740/757/771 nm (SIF_{683} , SIF_{740} , SIF_{757} , and SIF_{771} , respectively), normalized difference vegetation index (NDVI) and enhanced vegetation index (EVI) (A. R. Huete et al., 1997; A. Huete et al., 2002; Tucker, 1979), and NIRv (Badgley et al., 2017):

$$NDVI = \frac{\alpha_{NIR} - \alpha_{RED}}{\alpha_{NIR} + \alpha_{RED}}, \quad (3)$$

$$EVI = 2.5 \cdot \frac{\alpha_{NIR} - \alpha_{RED}}{\alpha_{NIR} + 6 \cdot \alpha_{RED} - 7.5 \cdot \alpha_{BLUE} + 1}, \quad (4)$$

$$NIRv = NDVI \cdot \alpha_{NIR}, \quad (5)$$

where α is the top-of-canopy reflectance at the given wavelength from the viewing direction (BLUE: 469 nm, RED: 645 nm, and NIR: 858.5 nm). We output the canopy optical properties at a nadir viewing direction as there is no overpass satellite for most of the simulations. We ran our model for the year 2019 for full year record of TROPospheric Monitoring Instrument (TROPOMI), Orbiting Carbon Observatory 2 (OCO-2), and MODIS satellites, and the year 2010 for comparison with another latent heat flux data set (see Section 2.3). Per 1° grid, we re-sampled the hourly simulation to daily means (nighttime GPP and SIF values were counted as 0; nighttime time reflectance indices were not available and thus excluded). We further re-sampled the daily means to 8-daily, monthly, and annual means. We refer the readers to Y. Wang (2023b) daily, 8-daily, monthly, and annual mean CliMA GPP, SIF, and NIRv for the year 2010 and 2019.

2.3. Evaluation Data Sets

2.3.1. GPP and T

We compared CliMA Land predicted global GPP for year 2019 against the a data-driven GPP product interpolated from flux towers (MPI GPP; data from Tramontana et al., 2016). We selected the monthly mean 0.5° MPI GPP at year 2019 that was based on (a) ensembles that include GPP and terrestrial ecosystem respiration from all flux partitioning methods, (b) ensembles that include carbon fluxes from all machine learning methods, and (c) all carbon fluxes from remote sensing, RS (RS GPP does not use meteorological forcing data). The data was labeled as “GPP.RS_V006.FP-ALL.MLM-ALL.METEO-NONE” as noted at <https://www.fluxcom.org/CF-Download/>. We regridded the MPI GPP to 1° and retained its temporal resolution. It is worth noting that the MPI GPP is a machine-learning based upscaling of flux tower derived GPP from sparsely distributed towers (not true measurements), and that we compared CliMA GPP to this reference data set rather than to flux tower derived GPP directly (as the towers do not cover the entire grid cell).

We compared CliMA Land modeled T for the year 2010 against the latent heat flux (LE) product interpolated from flux towers (Jung et al., 2019). The data was labeled as “LE.RS.EBC-ALL.MLM-ALL.METEO-NONE” as noted at <https://www.fluxcom.org/EF-Download/>. Note that the MPI LE data sets were for total evapotranspiration (including T, and evaporation from leaf surface and soil), thus we used this product only to roughly test whether the modeled T captures the spatial patterns.

2.3.2. SIF

We compared CliMA Land predicted mean SIF_{683} and SIF_{740} to the daily average SIF_{683} and SIF_{740} retrievals from TROPOMI (data from Köhler et al., 2018; Köhler et al., 2020). We compare CliMA mean SIF_{757} and SIF_{771} to the daily average SIF_{757} and SIF_{771} retrievals from the Orbiting Carbon Observatory 2, OCO-2 (Sun et al., 2017). Note here that TROPOMI and OCO-2 SIF were averaged from observations with different sun-sensor geometries and that the day length correction was made with the assumption that SIF is function of the cosine of the solar zenith angle. In comparison, CliMA SIF was modeled at nadir direction (viewing zenith angle is 0°), and the day length correction was made by averaging all modeled SIF at different times of a day (solar zenith angle changes with time).

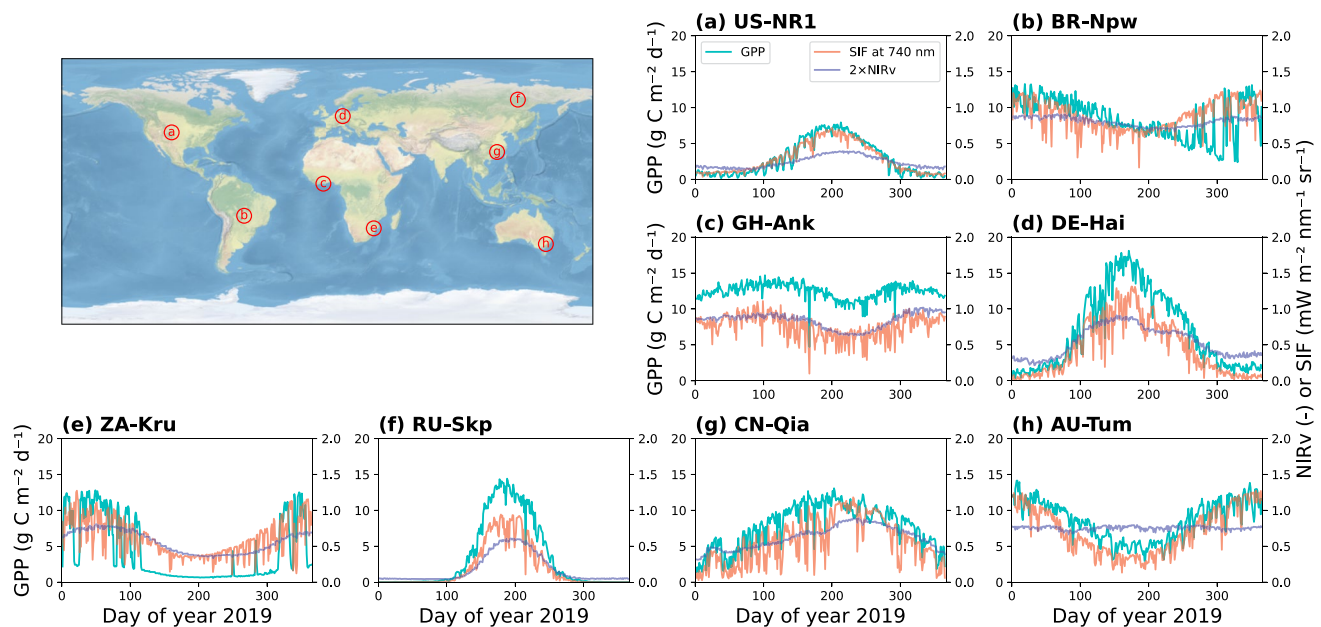


Figure 2. Examples of Climate Modeling Alliance (CliMA) Land run at eight 1° grid cells across the globe. CliMA Land global run was made for year 2019. The (latitude, longitude) centers are (a) $(40.5^\circ, -105.5^\circ)$, (b) $(-16.5^\circ, -56.5^\circ)$, (c) $(5.5^\circ, -2.5^\circ)$, (d) $(51.5^\circ, 10.5^\circ)$, (e) $(-25.5^\circ, 31.5^\circ)$, (f) $(62.5^\circ, 129.5^\circ)$, (g) $(26.5^\circ, 115.5^\circ)$, and (h) $(-35.5^\circ, 148.5^\circ)$, respectively. There is a flux tower within each example grid cell, and they are US-NR1, BR-Npw, GH-Ank, DE-Hai, ZA-Kru, RU-Skp, CN-Qia, and AU-Tum, respectively. The cyan curve plots the modeled daily cumulative gross primary productivity; the red curve plots the modeled daily mean solar-induced chlorophyll fluorescence at 740 nm; the blue curve plots the modeled daytime mean near infrared reflectance of vegetation (NIRv). NIRv is scaled to 2 times the original value to facilitate visualization.

2.3.3. NDVI, EVI, and NIRv

We compared CliMA Land predicted NDVI, EVI, and NIRv to those retrieved using the MODIS satellites MCD43A4 v006 data set (original spatial resolution is ~ 500 m) (Schaaf & Wang, 2015). Note that MODIS MCD43A4 v006 reflectance data have been corrected to nadir direction, which agrees with CliMA Land simulations. We regridded the MODIS MCD43A4 v006 to global scale NDVI, EVI, and NIRv with 1° spatial resolution and 8 day temporal resolution (first computing the indices for each data point falls in the grid, then taking the average of the computed indices).

3. Results

3.1. Seasonal Cycles

Our model simulation captured the overall seasonality of GPP, SIF, and NIRv (e.g., peaks in the middle of the year in the northern hemisphere; Figure 2). In general, the simulated SIF and NIRv tracked the simulated variations of GPP well for the eight selected grid cells with flux towers located within. However, linear relationship between GPP and SIF were particularly weak in grid cells b and c (Table 4) because of a drought in grid cell b (days 150–350) and lack of clear seasonality in SIF for grid cell c. As to NIRv, we found weak linear relationship with GPP in grid cell h due to the lack of seasonality in NIRv.

Our model simulation suggested that none of the SIF, NDVI, EVI, or NIRv over-competed the others in capturing the GPP seasonality (in daily time scale). For the eight example grid cells in Figure 2, SIF/NDVI/EVI/NIRv each had the highest R^2 in 3/3/0/2 grid cells when linearly correlated to GPP, respectively (Table 4). Modeled SIF at four wavelengths all showed reasonably well correlation with NIRv except grid cell h, where NIRv showed little seasonality. Further, for all example grid cells, R^2 between SIF_{683} and NIRv was lower than that for SIF_{740} , SIF_{757} , and SIF_{771} (Table 4); this was likely caused by SIF reabsorption in the red light region.

3.2. Spatial Patterns

Compared to the nine benchmark products of GPP, T, SIF, and vegetation indices, CliMA Land modeled quantities all displayed reasonable spatial patterns across the globe (in terms of annual mean comparison), though the magnitudes differed (see Figure 3 for examples of GPP, SIF_{740} , NIRv, Figure 4).

Table 4
Coefficient of Determination Among Climate Modeling Alliance Land Modeled Quantities in Eight Grid Cells

Site	US-NR1	BR-Npw	GH-Ank	DE-Hai	ZA-Kru	RU-Skp	CN-Qia	AU-Tum
GPP-SIF ₆₈₃	0.935	0.002	0.297	0.870	0.223	0.877	0.697	0.800
GPP-SIF ₇₄₀	0.954	0.003	0.275	0.917	0.243	0.951	0.701	0.788
GPP-SIF ₇₅₇	0.954	0.003	0.284	0.920	0.246	0.950	0.693	0.790
GPP-SIF ₇₇₁	0.953	0.003	0.288	0.920	0.247	0.949	0.690	0.791
GPP-NDVI	0.887	0.360	0.389	0.820	0.525	0.949	0.736	0.167
GPP-EVI	0.861	0.283	0.321	0.889	0.553	0.959	0.675	0.003
GPP-NIRv	0.877	0.277	0.292	0.906	0.557	0.960	0.653	0.003
SIF ₆₈₃ -NIRv	0.800	0.325	0.326	0.796	0.435	0.778	0.530	0.015
SIF ₇₄₀ -NIRv	0.883	0.408	0.465	0.860	0.502	0.904	0.728	0.026
SIF ₇₅₇ -NIRv	0.886	0.434	0.509	0.860	0.508	0.905	0.744	0.027
SIF ₇₇₁ -NIRv	0.887	0.443	0.525	0.860	0.509	0.905	0.749	0.027

Note. The number is R^2 of the linear regression of daily means (very low R^2 marked with shaded red). The row "Site" indicates that there is a flux tower located within the grid cell.

Our modeled quantities, in general, were higher than the benchmark data sets. The disagreements were likely due to (a) that we have not calibrated the model, and (b) that benchmark data sets have systematic errors. For example, CliMA SIF was generally higher than TROPOMI and OCO-2 SIF (Figure 4), as simulated SIF is positive by construction whereas space-borne retrievals can be negative. Overall, CliMA Land simulations showed better agreements with MODIS reflectance than TROPOMI and OCO SIF (Figure 4), suggesting the necessity to use SIF to calibrate the model inputs (chlorophyll content retrieval was based on MODIS).

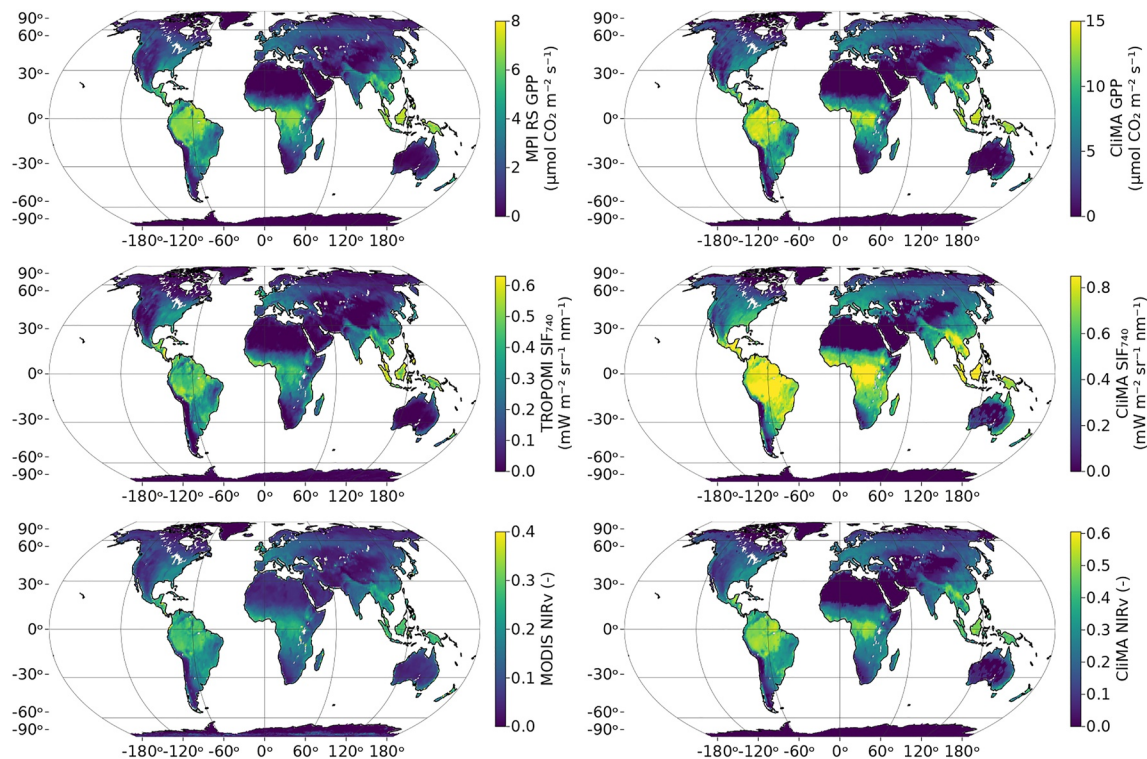


Figure 3. Comparison of Climate Modeling Alliance Land predicted quantities to benchmark data sets. Shown examples included gross primary productivity, solar-induced chlorophyll fluorescence at 740 nm, and near infrared reflectance of vegetation. All comparisons are made for the year 2019.

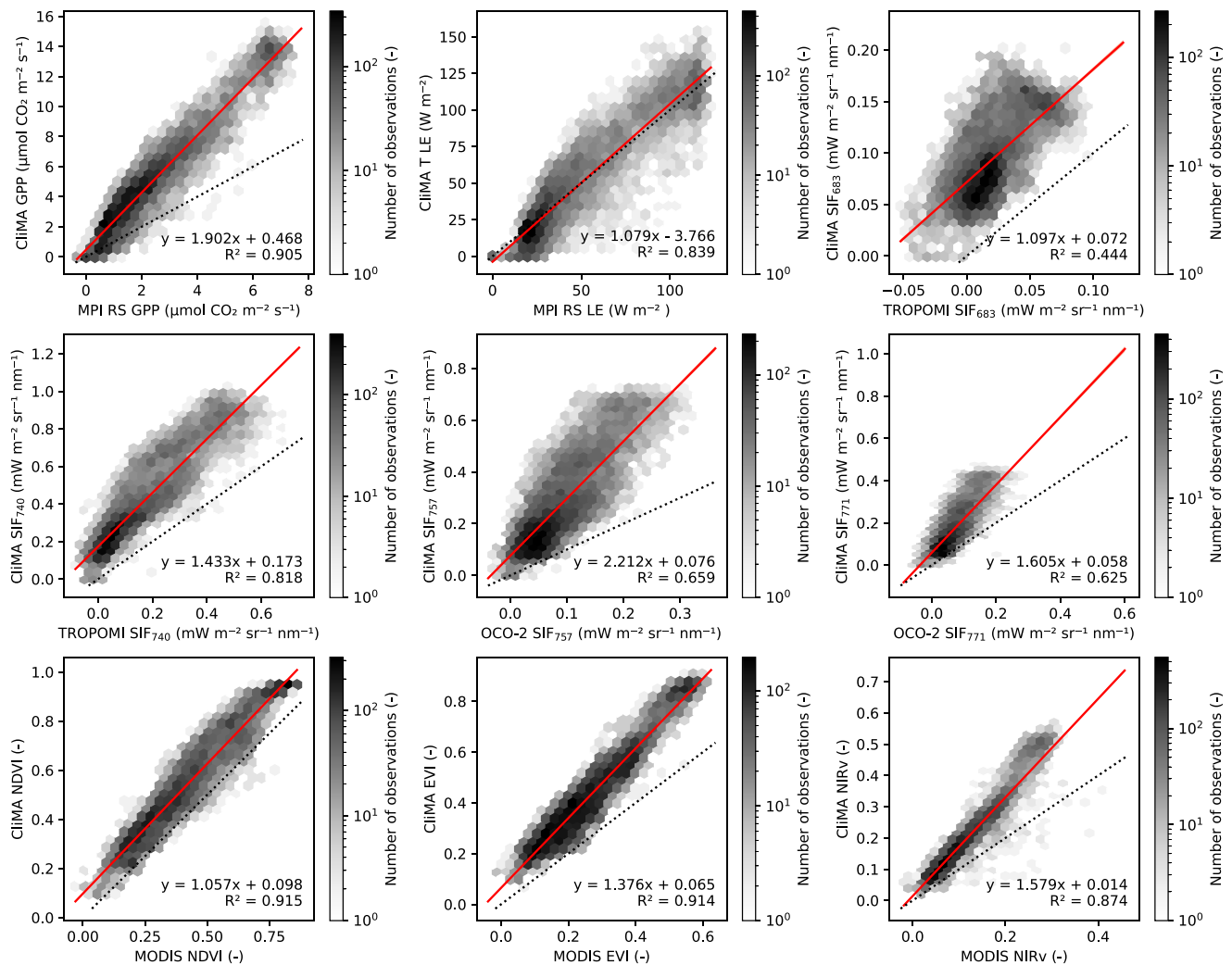


Figure 4. Comparison of Climate Modeling Alliance (Clima) Land predicted quantities to benchmark data sets. Shown comparisons are made for annual means. Red solid line plots the linear regression, and black dotted line plots the 1:1 line. Note that CIMA latent heat flux (LE) used in the comparison is from vegetation transpiration only whereas MPI RS LE used also include leaf surface and soil evaporation. The comparison for LE is made for the year 2010, whereas the rest are made for the year 2019.

4. Discussion

We present and evaluate CIMA Land, an in-development LSM that aims to simultaneously simulate hyperspectral canopy fluorescence and reflectance properties as well as corresponded vegetation GPP and T. CIMA Land modeled fluxes and indices, in general, well captured the spatial patterns globally compared to (a) MPI RS GPP and LE, (b) TROPOMI and OCO-2 SIF, and (c) MODIS NDVI, EVI, and NIRv, though the magnitude differed.

4.1. Correlations Among GPP, SIF, and NIRv

SIF and NIRv are often used as proxy for GPP given their correlations to PAR, and their inter-correlations are highest when the seasonality matches (Figures 2a and 2d–2f). Although SIF is proportional to absorbed PAR and fluorescence quantum yield and the latter decreases during a drought, sensitivity of SIF to drought is way lower than that of GPP (Helm et al., 2020). Therefore, it is expected to see SIF increases during a drought when PAR increases faster than the decline of fluorescence quantum yield (e.g., Figures 2b, 5a, and 5b). NIRv is mostly determined by canopy structure, leaf pigments, and sun-sensor geometry, and thus can only be used to proxy GPP when its seasonality matches those of drought and PAR (e.g., Figures 2a, 2c, 2d, 2f, and 2g). Thus, although SIF and NIRv have shown great potential in projecting global patterns of GPP (Badgley et al., 2017; Sun et al., 2017),

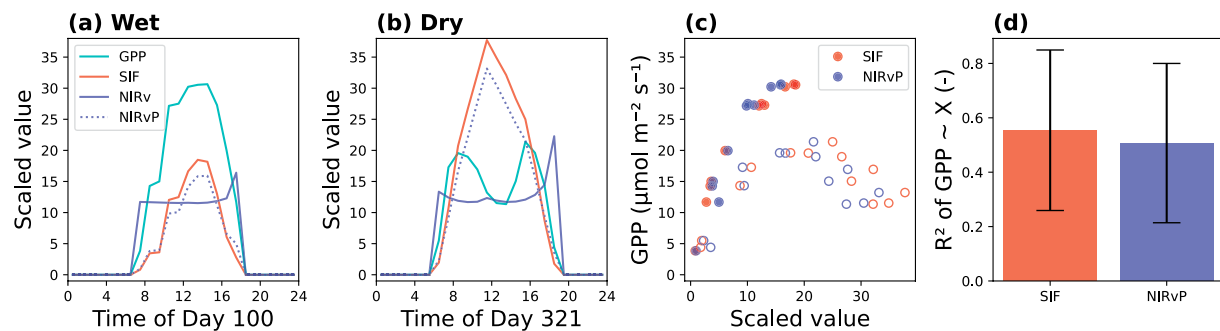


Figure 5. Comparison of Climate Modeling Alliance Land predicted quantities in a diurnal cycle. (a) Diurnal cycles of gross primary productivity (GPP), solar-induced chlorophyll fluorescence (SIF), near infrared reflectance of vegetation (NIRv), and NIRvP in day 100 when soil is wet. GPP is not scaled, SIF (at 740 nm, $\text{mW m}^{-2} \text{nm}^{-1} \text{sr}^{-1}$) is scaled by 10 times, NIRv (unitless) is scaled by 30 times, NIRvP ($\mu\text{mol m}^{-2} \text{s}^{-1}$) is scaled to 1/25. (b) Diurnal cycles in day 321 when soil is dry. (c) Correlation between GPP versus SIF and NIRvP. Closed symbols plot the values from panel a, and open symbols plot the values from panel (b). (d) Comparison of R^2 of GPP versus SIF and NIRvP. The bars plot the mean R^2 for all the days in year 2019, and the error bars plot the standard deviation of R^2 . R^2 is computed by fitting the model simulated quantities in a diurnal cycle.

they are not guaranteed to be a good proxy for GPP seasonality at site or grid level (Doughty et al., 2021), particularly when there is a drought (e.g., days 150–350 in Figure 2b; Marengo et al. (2021)).

In a diurnal cycle, canopy SIF is positively correlated to PAR, thus a good correlation with GPP is expected when plants are not stressed (see an example in Figures 5a and 5c). However, if the plants are under a drought stress, higher PAR and the accompanied drier and warmer air would result in lower GPP but subtle change in SIF. In this case, it is expected to see decoupling of SIF and GPP at high PAR (see an example in Figures 5b and 5c). In comparison, as NIRv is a unitless index based on canopy reflectance, it barely changes in a diurnal cycle except for in the early morning and late afternoon when solar zenith angle is high (Figure 5). Given this, NIRv is often scaled by a radiation measure to better account for the impact from PAR, for example, Wu et al. (2020) scaled SIF by incoming near infrared radiation Dechant et al. (2022) scaled NIRv by incoming PAR. When we scaled NIRv by incoming PAR (NIRvP), we indeed found a more realistic NIRvP diurnal cycle at both wet and dry conditions. However, similar to SIF, NIRvP also showed weak correlation with GPP in dry environment. Thus, as suggested by Figure 5, using SIF or NIRvP to track GPP diurnal cycles should be constrained to the scenario of non-stressed environment.

Note here that fluorescence quantum yield decreases with higher PAR, hence resulting in slower SIF increase than PAR. As GPP tends to saturate at higher PAR, it is expected that SIF shows a better theoretical correlation with GPP in diurnal cycles than NIRvP (Figure 5d). However, the better theoretical performance of SIF in tracking diurnal cycles of GPP than NIRvP may not be detected in observations as the noise-to-signal ratio is much higher in SIF retrievals.

4.2. Future Steps to Improve CliMA Land

CliMA Land is not well constrained or calibrated given the various sources of plant traits and environmental cues. First, the input data sets often disagree in their assumptions and model complexity, likely resulting in biases in simulated results (Y. Wang & Frankenberg, 2022a). Second, because of the limited knowledge of how plant physiological traits vary spatially and temporally, data sets used to drive CliMA Land are often temporally constant instead of a time series. For instance, photosynthetic capacity represented by $V_{\text{cmax}25}$, which should be varying in a growing season, is constant in a grid cell in our simulation, and this might contribute biases in the simulated carbon and water fluxes (Y. P. Wang et al., 2007). Further, the vertical gradients of traits within the canopy was not considered in the present study, such as the chlorophyll content. Also, the ratio between carotenoid and chlorophyll can be highly variable. Future research aiming to quantitatively understand the vertical canopy layout (such as optimal nutrient and leaf area partitioning) and their spatial and temporal variability will improve the predictive skills of CliMA Land. Third, CliMA Land prescribed environmental cues regridded from ERA5 reanalysis data, which were interpolated from sparsely distributed historical observations and could have high uncertainty; and mismatch between our regridded ERA5 reanalysis data and reality would also contribute to biases in our model output. For example, when comparing the soil water contents from our regridded ERA5

reanalysis (black curve in Figure S1 in Supporting Information S1) versus that from flux tower measurements (red curve with shaded region in Figure S1 in Supporting Information S1), we found that our regridded ERA5 reanalysis data had wetter soil throughout the year, particularly from day 1–150, which corresponded to the growing season at AU-Tum. Promisingly, with the increasing number of observations across the globe, the uncertainty and biases resulting from model parameter and resolution mismatch will be better resolved in the future (Cucchi et al., 2020).

Some key processes have been missing in the global-scale LSMs, such as the dynamics and variations in leaf photosynthesis and fluorescence related physiology. For example, Magney et al. (2019) and Raczka et al. (2019) highlighted the importance of sustained non-photochemical quenching (NPQ) in modeling SIF in the cold winter, which results in lower modeled SIF in cold environments. However, this process has not been yet implemented in any land surface or vegetation model (including CliMA Land) because of the lack of knowledge on how sustained NPQ quantitatively and mechanistically responds to temperature. Also, we used constant parameter sets for rate coefficient calculations such as the temperature dependency of maximum carboxylation rate, whereas species-dependent parameter sets (Medlyn et al., 2002) should be used to best describe plants' acclimation to the environment. Similarly, the fluorescence parameter set we used to compute NPQ, fluorescence yield, and hence SIF (see van der Tol et al. (2014) for more details), was also constant across the globe, regardless of the site-level species composition and stress status. Future research efforts to implement new physiological processes and resolve the spatial and temporal variations and acclimation of these physiological parameters will also improve the predictive skills of LSMs.

The global scale data-driven GPP estimation used in the present study was interpolated using machine learning based on algorithms, and thus had high uncertainty in the grid cells without a flux tower. Further, even for those grid cells with flux towers, there could be issues when upscaling flux tower observations that typically covers <1 km² footprint to the entire grid cell that may range up to >10,000 km² and consist various species with contrasting traits. Yet, the variations within a grid were not well represented in neither MPI GPP nor CliMA Land. A recent study compared 45 global GPP products and found considerable difference among the products, and the annual GPP ranges from approximately 0.8 to 2.4 times the MPI GPP (Zhang & Ye, 2021). In comparison, CliMA GPP was 1.87 times the MPI RS GPP for the year 2019. Therefore, as true global GPP patterns are unknown and current estimates are highly inconsistent (Anav et al., 2015; Zhang & Ye, 2021), effective evaluation of CliMA GPP or any other GPP remains a challenge.

The global-scale TROPOMI, OCO-2, and MODIS observations may have considerable systematic errors. For comparison with MODIS data, the error may arise from (a) the bidirectional reflectance distribution function used by MODIS and CliMA Land are different (Schaaf & Wang, 2015), (b) CliMA Land canopy reflectance is computed based on the prescribed top of canopy radiation and there is not an extra step to correct atmosphere absorption, whereas MODIS reflectance needs to make correction for both top of canopy radiation and canopy reflected radiation. For comparison of SIF, the retrievals are often negative or close to zero, particularly in those regions with low vegetation cover, making it difficult for a 1:1 comparison between CliMA Land output and satellite observations. As a result, there is always a positive offset in the linear regressions. For example, SIF retrieval may use barren land as a baseline, and the potential illuminance from other chemicals other than chlorophyll could lead to biases over the baseline (Köhler et al., 2021). Moreover, the mismatch in spatial resolution of the soundings, sampling frequency, and sun-sensor geometry likely impacted the 1:1 comparison between CliMA Land and TROPOMI/OCO-2 SIF. We note that the daily average SIF in CliMA Land was calculated by averaging the SIF at nadir throughout the diurnal cycle (as there is no overpass satellite for most of the simulations), whereas TROPOMI/OCO-2 daily mean SIF was converted from point measurements with varying solar zenith angles based on an assumption that SIF is a function of cosine solar zenith angle that peaks at midday, which may not be true. We note that CliMA Land allows for using specific sun-sensor geometry and solar time that match all satellite overpasses, enabling the direct comparison between model simulation and satellite retrievals rather than the averages (as done in Figure 16 of Y. Wang et al., 2021). As CliMA Land can simulate canopy optical properties and vegetation GPP and T at the time, it allows for more systematic and comprehensive model calibration using data from multiple sources (Fox et al., 2018; Kaminski et al., 2013; Smith et al., 2020), thus promoting future research on plant trait inversion at various spatial and temporal resolutions.

As we aim to present an overview of the CliMA Land global simulation, we ran the model at relatively coarse spatial resolution at 1°. In each 1° grid cell, we used mean values for all input parameters to drive the model

simulation, and this could result in uncertainties due to the nonlinear relationships among vegetation processes (such as stomatal behavior and soil moisture). Further, we assumed each 1° grid cell as a site with bulk properties, and ignored the heterogeneity of species distribution and/or vertical canopy structure (upper canopy and lower canopy). Future simulations at high spatial resolution using CliMA Land after we calibrate the model with various data could resolve this problem.

We note that CliMA predictions (pure forward model run without parameter calibration) were generally higher than existing MPI, TROPOMI, OCO-2, and MODIS products. Aside from errors in the reference benchmark data sets, the differences probably resulted from non-idealized model parameter configuration, such as chlorophyll content which was not inverted to use with a hyperspectral and multi-layer canopy RT scheme (so did many other input parameters). For example, if we use a lower chlorophyll content in the model, the vegetation will be less greener and thus NDVI, EVI, and NIRv will be lower; SIF and GPP will also be lower given the lower PAR absorption. Being able to simultaneously model hyperspectral canopy RT as well as carbon and water fluxes, CliMA Land has great potential in advancing future Earth System modeling. The simulated hyperspectral canopy RT can be directly compared to satellite observations, and can help constrain the Earth system model with the large number of remote sensing data such as inverting chlorophyll content that (a) is compatible with hyperspectral and multi-layer canopy RT scheme, and (b) agrees with remote sensing and/or ground-based data from multiple sources. This way, the model predicted GPP would have higher confidence than those calibrated with limited data sources (Croft et al., 2020).

Further, the high temporal resolution of CliMA Land outputs provides an improved way to interpolate observations using modeled patterns (e.g., one can simulate the SIF diurnal cycles and then use it to scale SIF, rather than using a cosine function of solar zenith angle). The global scales simulations allow for novel research that was not feasible in the past, such as the decoupling of SIF and NIRv versus GPP in a diurnal cycle under different environmental stresses, supplementing the deficits of traditional satellite retrievals. We believe that future global maps of hyperspectral data with improved temporal resolutions, for example, the NASA Surface Biology and Geology (SBG) mission (Cawse-Nicholson et al., 2021) and the NASA Earth Surface Mineral Dust Source Investigation (EMIT), can be used as model inputs, and that the implementation of new features and better representations into the land model will advance the model predictive skills, for not only the past but also the future climate with respect to global climate change.

5. Conclusions

We present an overview and our first global run of CliMA Land, a LSM that outputs carbon and water fluxes as well as hyperspectral canopy reflectance and fluorescence simultaneously. We compare the model outputs to other data-driven GPP, SIF, NDVI, EVI, and NIRv products, and demonstrate the potential of CliMA Land in tracking their spatial patterns. Our model simulations underline (a) the necessity of improving model parameter configuration of the new model, both spatially and temporally; (b) the importance of implementing more advanced or new features; and (c) the demand of integrating data sets to calibrate the model.

Data Availability Statement

The global scale data sets used for CliMA Land simulation (except for ERA5 data) can be accessed through Grid-Machine (<https://github.com/CliMA/GriddingMachine.jl>; Y. Wang et al., 2022). The exact version of CliMA Land used in the present study can be found at (Y. Wang, 2023a), and the model outputs for years 2010 and 2019 are archived at Zenodo (Y. Wang, 2023b).

References

- Anav, A., Friedlingstein, P., Beer, C., Ciais, P., Harper, A., Jones, C., et al. (2015). Spatiotemporal patterns of terrestrial gross primary production: A review. *Reviews of Geophysics*, 53(3), 785–818. <https://doi.org/10.1002/2015rg000483>
- Anav, A., Friedlingstein, P., Kidston, M., Bopp, L., Ciais, P., Cox, P., et al. (2013). Evaluating the land and ocean components of the global carbon cycle in the CMIP5 earth system models. *Journal of Climate*, 26(18), 6801–6843. <https://doi.org/10.1175/jcli-d-12-00417.1>
- Anderegg, W. R., Wolf, A., Arango-Velez, A., Choat, B., Chmura, D. J., Jansen, S., et al. (2018). Woody plants optimise stomatal behaviour relative to hydraulic risk. *Ecology Letters*, 21(7), 968–977. <https://doi.org/10.1111/ele.12962>
- Anderegg, W. R. L., Schwalm, C., Biondi, F., Camarero, J. J., Koch, G., Litvak, M., et al. (2015). Pervasive drought legacies in forest ecosystems and their implications for carbon cycle models. *Science*, 349(6247), 528–532. <https://doi.org/10.1126/science.aab1833>

Acknowledgments

We gratefully acknowledge the generous support of Eric and Wendy Schmidt (by recommendation of the Schmidt Futures) and the Heising-Simons Foundation. This research has been supported by the National Aeronautics and Space Administration (NASA) Earth Sciences Division grant NNX15AH95G and NASA Carbon Cycle Science Grant 80NSSC21K1712 awarded to Christian Frankenberg. M.L. was supported by the NASA Postdoctoral Program, administered by Universities Space Research Association under contract with NASA, and by the Next Generation Ecosystem Experiments-Tropics, funded by the U.S. Department of Energy, Office of Science, Office of Biological and Environmental Research. We gratefully thank Dr. Butler, Croft, Dai, He, Lawrence, Luo, Simard, Yamazaka, and Yuan for sharing the gridded data sets. We gratefully thank the expert reviewers for their highly constructive suggestions. ERA5 data were generated using Copernicus Climate Change Service Information. Neither the European Commission nor the European Centre for Medium-Range Weather Forecasts (ECMWF) are responsible for any use that may be made of the Copernicus information or data in this publication. Part of this research was carried out at the Jet Propulsion Laboratory, California Institute of Technology, under a contract with NASA. California Institute of Technology. Government sponsorship acknowledged. © 2023. All rights reserved.

- Arora, V. K., Boer, G. J., Friedlingstein, P., Eby, M., Jones, C. D., Christian, J. R., et al. (2013). Carbon–concentration and carbon–climate feedbacks in CMIP5 earth system models. *Journal of Climate*, 26(15), 5289–5314. <https://doi.org/10.1175/jcli-d-12-00494.1>
- Bacour, C., Maignan, F., MacBean, N., Porcar-Castell, A., Flexas, J., Frankenberg, C., et al. (2019). Improving estimates of gross primary productivity by assimilating solar-induced fluorescence satellite retrievals in a terrestrial biosphere model using a process-based sif model. *Journal of Geophysical Research: Biogeosciences*, 124(11), 3281–3306. <https://doi.org/10.1029/2019jg005040>
- Badgley, G., Anderegg, L. D., Berry, J. A., & Field, C. B. (2019). Terrestrial gross primary production: Using NIR_v to scale from site to globe. *Global Change Biology*, 25(11), 3731–3740. <https://doi.org/10.1111/gcb.14729>
- Badgley, G., Field, C. B., & Berry, J. A. (2017). Canopy near-infrared reflectance and terrestrial photosynthesis. *Science Advances*, 3(3), e1602244. <https://doi.org/10.1126/sciadv.1602244>
- Baldocchi, D. D. (2020). How eddy covariance flux measurements have contributed to our understanding of global change biology. *Global Change Biology*, 26(1), 242–260. <https://doi.org/10.1111/gcb.14807>
- Baldocchi, D. D., Falge, E., Gu, L., Olson, R., Hollinger, D., Running, S., et al. (2001). FLUXNET: A new tool to study the temporal and spatial variability of ecosystem-scale carbon dioxide, water vapor, and energy flux densities. *Bulletin of the American Meteorological Society*, 82(11), 2415–2434. [https://doi.org/10.1175/1520-0477\(2001\)082<2415:fants>2.3.co;2](https://doi.org/10.1175/1520-0477(2001)082<2415:fants>2.3.co;2)
- Ball, J. T., Woodrow, I. E., & Berry, J. A. (1987). A model predicting stomatal conductance and its contribution to the control of photosynthesis under different environmental conditions. In *Progress in photosynthesis research* (pp. 221–224). Springer.
- Bezanson, J., Edelman, A., Karpinski, S., & Shah, V. B. (2017). Julia: A fresh approach to numerical computing. *SIAM Review*, 59(1), 65–98. <https://doi.org/10.1137/141000671>
- Bonan, G. B., Patton, E. G., Finnigan, J. J., Baldocchi, D. D., & Harman, I. N. (2021). Moving beyond the incorrect but useful paradigm: Reevaluating big-leaf and multilayer plant canopies to model biosphere-atmosphere fluxes—a review. *Agricultural and Forest Meteorology*, 306, 108435. <https://doi.org/10.1016/j.agrformet.2021.108435>
- Bonan, G. B., Patton, E. G., Harman, I. N., Oleson, K. W., Finnigan, J. J., Lu, Y., & Burakowski, E. A. (2018). Modeling canopy-induced turbulence in the Earth system: A unified parameterization of turbulent exchange within plant canopies and the roughness sublayer (CLM-ml v0). *Geoscientific Model Development*, 11(4), 1467–1496. <https://doi.org/10.5194/gmd-11-1467-2018>
- Braghiere, R. K., Quaife, T., Black, E., He, L., & Chen, J. (2019). Underestimation of global photosynthesis in earth system models due to representation of vegetation structure. *Global Biogeochemical Cycles*, 33(11), 1358–1369. <https://doi.org/10.1029/2018gb006135>
- Braghiere, R. K., Quaife, T., Black, E., Ryu, Y., Chen, Q., De Kauwe, M. G., & Baldocchi, D. (2020). Influence of sun zenith angle on canopy clumping and the resulting impacts on photosynthesis. *Agricultural and Forest Meteorology*, 291, 108065. <https://doi.org/10.1016/j.agrformet.2020.108065>
- Braghiere, R. K., Wang, Y., Doughty, R., Sousa, D., Magney, T., Widlowski, J.-L., et al. (2021). Accounting for canopy structure improves hyperspectral radiative transfer and sun-induced chlorophyll fluorescence representations in a new generation Earth system model. *Remote Sensing of Environment*, 261, 112497. <https://doi.org/10.1016/j.rse.2021.112497>
- Butler, E. E., Datta, A., Flores-Moreno, H., Chen, M., Wythers, K. R., Fazayeli, F., et al. (2017). Mapping local and global variability in plant trait distributions. *Proceedings of the National Academy of Sciences*, 114(51), E10937–E10946. <https://doi.org/10.1073/pnas.1708984114>
- Campbell, G. S., & Norman, J. M. (1998). *An introduction to environmental biophysics*. Springer Science & Business Media.
- Cawse-Nicholson, K., Townsend, P. A., Schimel, D., Assiri, A. M., Blake, P. L., Buongiorno, M. F., et al. (2021). NASA's surface biology and geology designated observable: A perspective on surface imaging algorithms. *Remote Sensing of Environment*, 257, 112349. <https://doi.org/10.1016/j.rse.2021.112349>
- Collatz, G. J., Ribas-Carbo, M., & Berry, J. (1992). Coupled photosynthesis-stomatal conductance model for leaves of c4 plants. *Functional Plant Biology*, 19(5), 519–538. <https://doi.org/10.1071/pp9920519>
- Croft, H., Chen, J., Wang, R., Mo, G., Luo, S., Luo, X., et al. (2020). The global distribution of leaf chlorophyll content. *Remote Sensing of Environment*, 236, 111479. <https://doi.org/10.1016/j.rse.2019.111479>
- Cucchi, M., Weedon, G. P., Amici, A., Bellouin, N., Lange, S., Müller Schmied, H., et al. (2020). WFDE5: Bias-adjusted ERA5 reanalysis data for impact studies. *Earth System Science Data*, 12(3), 2097–2120. <https://doi.org/10.5194/essd-12-2097-2020>
- Dai, Y., Xin, Q., Wei, N., Zhang, Y., Shangquan, W., Yuan, H., et al. (2019). A global high-resolution data set of soil hydraulic and thermal properties for land surface modeling. *Journal of Advances in Modeling Earth Systems*, 11(9), 2996–3023. <https://doi.org/10.1029/2019ms001784>
- Dechant, B., Ryu, Y., Badgley, G., Köhler, P., Rascher, U., Migliavacca, M., et al. (2022). NIRvP: A robust structural proxy for sun-induced chlorophyll fluorescence and photosynthesis across scales. *Remote Sensing of Environment*, 268, 112763. <https://doi.org/10.1016/j.rse.2021.112763>
- De Kauwe, M. G., Kala, J., Lin, Y.-S., Pitman, A. J., Medlyn, B. E., Duursma, R. A., et al. (2015). A test of an optimal stomatal conductance scheme within the cable land surface model. *Geoscientific Model Development*, 8(2), 431–452. <https://doi.org/10.5194/gmd-8-431-2015>
- Doughty, R., Xiao, X., Köhler, P., Frankenberg, C., Qin, Y., Wu, X., et al. (2021). Global-scale consistency of spaceborne vegetation indices, chlorophyll fluorescence, and photosynthesis. *Journal of Geophysical Research: Biogeosciences*, 126(6), e2020JG006136. <https://doi.org/10.1029/2020jg006136>
- Eller, C. B., Rowland, L., Oliveira, R. S., Bittencourt, P. R. L., Barros, F. V., da Costa, A. C. L., et al. (2018). Modelling tropical forest responses to drought and El Niño with a stomatal optimization model based on xylem hydraulics. *Philosophical Transactions of the Royal Society B: Biological Sciences*, 373(1760), 20170315. <https://doi.org/10.1098/rstb.2017.0315>
- Farquhar, G. D., von Caemmerer, S., & Berry, J. A. (1980). A biochemical model of photosynthetic CO₂ assimilation in leaves of C₃ species. *Planta*, 149(1), 78–90. <https://doi.org/10.1007/bf00386231>
- Féret, J.-B., Gitelson, A., Noble, S., & Jacquemoud, S. (2017). PROSPECT-D: Towards modeling leaf optical properties through a complete lifecycle. *Remote Sensing of Environment*, 193, 204–215. <https://doi.org/10.1016/j.rse.2017.03.004>
- Fernández-Martínez, M., Sardans, J., Chevallier, F., Ciais, P., Obersteiner, M., Vicca, S., et al. (2019). Global trends in carbon sinks and their relationships with CO₂ and temperature. *Nature Climate Change*, 9(1), 73–79. <https://doi.org/10.1038/s41558-018-0367-7>
- Fox, A. M., Hoar, T. J., Anderson, J. L., Arellano, A. F., Smith, W. K., Litvak, M. E., et al. (2018). Evaluation of a data assimilation system for land surface models using CLM4.5. *Journal of Advances in Modeling Earth Systems*, 10(10), 2471–2494. <https://doi.org/10.1029/2018ms001362>
- Frankenberg, C., Fisher, J. B., Worden, J., Badgley, G., Saatchi, S. S., Lee, J.-E., et al. (2011). New global observations of the terrestrial carbon cycle from GOSAT: Patterns of plant fluorescence with gross primary productivity. *Geophysical Research Letters*, 38(17), L17706. <https://doi.org/10.1029/2011gl048738>
- Gentemann, C. L., Clayson, C. A., Brown, S., Lee, T., Parfitt, R., Farrar, J. T., et al. (2020). FluxSat: Measuring the ocean–atmosphere turbulent exchange of heat and moisture from space. *Remote Sensing*, 12(11), 1796. <https://doi.org/10.3390/rs12111796>
- He, L., Chen, J. M., Pisek, J., Schaaf, C. B., & Strahler, A. H. (2012). Global clumping index map derived from the modis brdf product. *Remote Sensing of Environment*, 119, 118–130. <https://doi.org/10.1016/j.rse.2011.12.008>

- Helm, L. T., Shi, H., Lerdau, M. T., & Yang, X. (2020). Solar-induced chlorophyll fluorescence and short-term photosynthetic response to drought. *Ecological Applications*, 30(5), e02101. <https://doi.org/10.1002/eap.2101>
- Hersbach, H., Bell, B., Berrisford, P., Biavati, G., Horányi, A., Muñoz Sabater, J., et al. (2018). ERA5 hourly data on single levels from 1959 to present [Dataset]. Copernicus Climate Change Service (C3S) Climate Data Store (CDS). <https://doi.org/10.24381/cds.adbb2d47>
- Huete, A., Didan, K., Miura, T., Rodriguez, E. P., Gao, X., & Ferreira, L. G. (2002). Overview of the radiometric and biophysical performance of the modis vegetation indices. *Remote Sensing of Environment*, 83(1–2), 195–213. [https://doi.org/10.1016/s0034-4257\(02\)00096-2](https://doi.org/10.1016/s0034-4257(02)00096-2)
- Huete, A. R., Liu, H., & van Leeuwen, W. J. (1997). The use of vegetation indices in forested regions: Issues of linearity and saturation. In *IGARSS'97. 1997 IEEE international geoscience and remote sensing symposium proceedings. Remote sensing—A scientific vision for sustainable development* (Vol. 4, pp. 1966–1968).
- Huntzinger, D., Schwalm, C., Wei, Y., Cook, R., Michalak, A., Schaefer, K., et al. (2021). NACP MsTMP: Global 0.5-degree model outputs in standard format, version 2.0 [Dataset]. ORNL DAAC, Oak Ridge, Tennessee, USA. <https://doi.org/10.3334/ORNLDAAAC/1599>
- Huntzinger, D. N., Schwalm, C., Michalak, A. M., Schaefer, K., King, A. W., Wei, Y., et al. (2013). The North American carbon program multi-scale synthesis and terrestrial model intercomparison project—Part 1: Overview and experimental design. *Geoscientific Model Development*, 6(6), 2121–2133. <https://doi.org/10.5194/gmd-6-2121-2013>
- Johnson, J., & Berry, J. (2021). The role of cytochrome b_6f in the control of steady-state photosynthesis: A conceptual and quantitative model. *Photosynthesis Research*, 148(3), 101–136. <https://doi.org/10.1007/s11202-021-00840-4>
- Jones, C., Robertson, E., Arora, V., Friedlingstein, P., Shevliakova, E., Bopp, L., et al. (2013). Twenty-first-century compatible CO₂ emissions and airborne fraction simulated by CMIP5 earth system models under four representative concentration pathways. *Journal of Climate*, 26(13), 4398–4413. <https://doi.org/10.1175/jcli-d-12-00554.1>
- Jung, M., Koirala, S., Weber, U., Ichii, K., Gans, F., Camps-Valls, G., et al. (2019). The FLUXCOM ensemble of global land-atmosphere energy fluxes. *Scientific Data*, 6(1), 74. <https://doi.org/10.1038/s41597-019-0076-8>
- Jung, M., Reichstein, M., Margolis, H. A., Cescatti, A., Richardson, A. D., Arain, M. A., et al. (2011). Global patterns of land-atmosphere fluxes of carbon dioxide, latent heat, and sensible heat derived from eddy covariance, satellite, and meteorological observations. *Journal of Geophysical Research*, 116(G3), G00J07. <https://doi.org/10.1029/2010jg001566>
- Jung, M., Schwalm, C., Migliavacca, M., Walthert, S., Camps-Valls, G., Koirala, S., et al. (2020). Scaling carbon fluxes from eddy covariance sites to globe: Synthesis and evaluation of the fluxcom approach. *Biogeosciences*, 17(5), 1343–1365. <https://doi.org/10.5194/bg-17-1343-2020>
- Kaminski, T., Knorr, W., Schürmann, G., Scholze, M., Rayner, P. J., Zaehle, S., et al. (2013). The BETHY/JSBACH carbon cycle data assimilation system: Experiences and challenges. *Journal of Geophysical Research: Biogeosciences*, 118(4), 1414–1426. <https://doi.org/10.1002/jgrg.20118>
- Kennedy, D., Swenson, S., Oleson, K. W., Lawrence, D. M., Fisher, R., Lola da Costa, A. C., & Gentile, P. (2019). Implementing plant hydraulics in the community land model, version 5. *Journal of Advances in Modeling Earth Systems*, 11(2), 485–513. <https://doi.org/10.1029/2018ms001500>
- Koffi, E. N., Rayner, P. J., Norton, A. J., Frankenberg, C., & Scholze, M. (2015). Investigating the usefulness of satellite-derived fluorescence data in inferring gross primary productivity within the carbon cycle data assimilation system. *Biogeosciences*, 12(13), 4067–4084. <https://doi.org/10.5194/bg-12-4067-2015>
- Köhler, P., Behrenfeld, M. J., Landgraf, J., Joiner, J., Magney, T. S., & Frankenberg, C. (2020). Global retrievals of solar-induced chlorophyll fluorescence at red wavelengths with TROPOMI. *Geophysical Research Letters*, 47(15), e2020GL087541. <https://doi.org/10.1029/2020GL087541>
- Köhler, P., Fischer, W. W., Rossman, G. R., Grotzinger, J. P., Dougherty, R., Wang, Y., et al. (2021). Mineral luminescence observed from space. *Geophysical Research Letters*, 48(19), e2021GL095227. <https://doi.org/10.1029/2021gl095227>
- Köhler, P., Frankenberg, C., Magney, T. S., Guanter, L., Joiner, J., & Landgraf, J. (2018). Global retrievals of solar-induced chlorophyll fluorescence with TROPOMI: First results and intersensor comparison to OCO-2. *Geophysical Research Letters*, 45(19), 10456–10463. <https://doi.org/10.1029/2018gl079031>
- Konings, A. G., Saatchi, S. S., Frankenberg, C., Keller, M., Leshy, V., Anderegg, W. R., et al. (2021). Detecting forest response to droughts with global observations of vegetation water content. *Global Change Biology*, 27(23), 6005–6024. <https://doi.org/10.1111/gcb.15872>
- Lawrence, P. J., & Chase, T. N. (2007). Representing a new modis consistent land surface in the community land model (CLM 3.0). *Journal of Geophysical Research*, 112(G1), G01023. <https://doi.org/10.1029/2006jg000168>
- Lee, J.-E., Berry, J. A., van der Tol, C., Yang, X., Guanter, L., Damm, A., et al. (2015). Simulations of chlorophyll fluorescence incorporated into the Community Land Model version 4. *Global Change Biology*, 21(9), 3469–3477. <https://doi.org/10.1111/gcb.12948>
- Le Quéré, C., Andrew, R. M., Friedlingstein, P., Sitch, S., Pongratz, J., Manning, A. C., et al. (2018). Global carbon budget 2017. *Earth System Science Data*, 10(1), 405–448. <https://doi.org/10.5194/essd-10-405-2018>
- Leuning, R. (1995). A critical appraisal of a combined stomatal-photosynthesis model for C₃ plants. *Plant, Cell and Environment*, 18(4), 339–355. <https://doi.org/10.1111/j.1365-3040.1995.tb00370.x>
- Li, F., Hao, D., Zhu, Q., Yuan, K., Braghieri, R. K., He, L., et al. (2022). Vegetation clumping modulates global photosynthesis through adjusting canopy light environment. *Global Change Biology*, 29(3), 731–746. <https://doi.org/10.1111/gcb.16503>
- Luo, X., Keenan, T. F., Chen, J. M., Croft, H., Colin Prentice, I., Smith, N. G., et al. (2021). Global variation in the fraction of leaf nitrogen allocated to photosynthesis. *Nature Communications*, 12(1), 4866. <https://doi.org/10.1038/s41467-021-25163-9>
- Magney, T. S., Bowling, D. R., Logan, B. A., Grossmann, K., Stutz, J., Blanken, P. D., et al. (2019). Mechanistic evidence for tracking the seasonality of photosynthesis with solar-induced fluorescence. *Proceedings of the National Academy of Sciences*, 116(24), 11640–11645. <https://doi.org/10.1073/pnas.1900278116>
- Marengo, J. A., Cunha, A. P., Cuatras, L. A., Deusdará Leal, K. R., Broedel, E., Seluchi, M. E., et al. (2021). Extreme drought in the Brazilian pantanal in 2019–2020: Characterization, causes, and impacts. *Frontiers in Water*, 3, 13. <https://doi.org/10.3389/frwa.2021.639204>
- Medlyn, B. E., Dreyer, E., Ellsworth, D., Forstreuter, M., Harley, P. C., Kirschbaum, M. U. F., et al. (2002). Temperature response of parameters of a biochemically based model of photosynthesis. II. A review of experimental data. *Plant, Cell and Environment*, 25(9), 1167–1179. <https://doi.org/10.1046/j.1365-3040.2002.00891.x>
- Medlyn, B. E., Duursma, R. A., Eamus, D., Ellsworth, D. S., Prentice, I. C., Barton, C. V. M., et al. (2011). Reconciling the optimal and empirical approaches to modelling stomatal conductance. *Global Change Biology*, 17(6), 2134–2144. <https://doi.org/10.1111/j.1365-2486.2010.02375.x>
- Medlyn, B. E., Duursma, R. A., & Zeppel, M. J. (2011). Forest productivity under climate change: A checklist for evaluating model studies. *Wiley Interdisciplinary Reviews: Climate Change*, 2(3), 332–355. <https://doi.org/10.1002/wcc.108>
- Norby, R. J., Gu, L., Haworth, I. C., Jensen, A. M., Turner, B. L., Walker, A. P., et al. (2017). Informing models through empirical relationships between foliar phosphorus, nitrogen and photosynthesis across diverse woody species in tropical forests of Panama. *New Phytologist*, 215(4), 1425–1437. <https://doi.org/10.1111/nph.14319>

- Norton, A. J., Rayner, P. J., Koffi, E. N., & Scholze, M. (2018). Assimilating solar-induced chlorophyll fluorescence into the terrestrial biosphere model bethy-scope v1.0: Model description and information content. *Geoscientific Model Development*, 11(4), 1517–1536. <https://doi.org/10.5194/gmd-11-1517-2018>
- Norton, A. J., Rayner, P. J., Koffi, E. N., Scholze, M., Silver, J. D., & Wang, Y.-P. (2019). Estimating global gross primary productivity using chlorophyll fluorescence and a data assimilation system with the bethy-scope model. *Biogeosciences*, 16(15), 3069–3093. <https://doi.org/10.5194/bg-16-3069-2019>
- O'Neill, B. C., Tebaldi, C., van Vuuren, D. P., Eyring, V., Friedlingstein, P., Hurtt, G., et al. (2016). The scenario model intercomparison project (ScenarioMIP) for CMIP6. *Geoscientific Model Development*, 9(9), 3461–3482. <https://doi.org/10.5194/gmd-9-3461-2016>
- Parazoo, N. C., Magney, T., Norton, A., Raczka, B., Bacour, C., Maignan, F., et al. (2020). Wide discrepancies in the magnitude and direction of modeled solar-induced chlorophyll fluorescence in response to light conditions. *Biogeosciences*, 17(13), 3733–3755. <https://doi.org/10.5194/bg-17-3733-2020>
- Pinty, B., Lavergne, T., Dickinson, R., Widlowski, J.-L., Gobron, N., & Verstraete, M. (2006). Simplifying the interaction of land surfaces with radiation for relating remote sensing products to climate models. *Journal of Geophysical Research*, 111(D2), D02116. <https://doi.org/10.1029/2005jd005952>
- Powell, T. L., Galbraith, D. R., Christoffersen, B. O., Harper, A., Imbuzeiro, H., Rowland, L., et al. (2013). Confronting model predictions of carbon fluxes with measurements of Amazon forests subjected to experimental drought. *New Phytologist*, 200(2), 350–365. <https://doi.org/10.1111/nph.12390>
- Qiu, B., Chen, J. M., Ju, W., Zhang, Q., & Zhang, Y. (2019). Simulating emission and scattering of solar-induced chlorophyll fluorescence at far-red band in global vegetation with different canopy structures. *Remote Sensing of Environment*, 233, 111373. <https://doi.org/10.1016/j.rse.2019.111373>
- Raczka, B., Porcar-Castell, A., Magney, T., Lee, J. E., Köhler, P., Frankenberg, C., et al. (2019). Sustained nonphotochemical quenching shapes the seasonal pattern of solar-induced fluorescence at a high-elevation evergreen forest. *Journal of Geophysical Research: Biogeosciences*, 124(7), 2005–2020. <https://doi.org/10.1029/2018jg004883>
- Reid, R. C., Prausnitz, J. M., & Poling, B. E. (1987). *The properties of gases and liquids*. McGraw Hill Book Co.
- Sabot, M. E., De Kauwe, M. G., Pitman, A. J., Medlyn, B. E., Ellsworth, D. S., Martin-StPaul, N., et al. (2022). One stomatal model to rule them all? Towards improved representation of carbon and water exchange in global models. *Journal of Advances in Modeling Earth Systems*, 14(4), e2021MS002761. <https://doi.org/10.1029/2021MS002761>
- Schaaf, C., & Wang, Z. (2015). MCD43A4 MODIS/Terra+Aqua BRDF/albedo nadir BRDF adjusted ref daily L3 global - 500m v006 [Dataset]. NASA EOSDIS Land Processes DAAC. <https://doi.org/10.5067/MODIS/MCD43A4.006>
- Schimel, D., Pavlick, R., Fisher, J. B., Asner, G. P., Saatchi, S., Townsend, P., et al. (2015). Observing terrestrial ecosystems and the carbon cycle from space. *Global Change Biology*, 21(5), 1762–1776. <https://doi.org/10.1111/gcb.12822>
- Schimel, D., Schneider, F. D., & JPL Carbon and Ecosystem Participants. (2019). Flux towers in the sky: Global ecology from space. *New Phytologist*, 224(2), 570–584. <https://doi.org/10.1111/nph.15934>
- Shiklomanov, A. N., Dietze, M. C., Fer, I., Viskari, T., & Serbin, S. P. (2021). Cutting out the middleman: Calibrating and validating a dynamic vegetation model (ED2-PROSPECT5) using remotely sensed surface reflectance. *Geoscientific Model Development*, 14(5), 2603–2633. <https://doi.org/10.5194/gmd-14-2603-2021>
- Sitch, S., Friedlingstein, P., Gruber, N., Jones, S. D., Murray-Tortarolo, G., Ahlström, A., et al. (2015). Recent trends and drivers of regional sources and sinks of carbon dioxide. *Biogeosciences*, 12(3), 653–679. <https://doi.org/10.5194/bg-12-653-2015>
- Smith, W. K., Fox, A. M., MacBean, N., Moore, D. J., & Parazoo, N. C. (2020). Constraining estimates of terrestrial carbon uptake: New opportunities using long-term satellite observations and data assimilation. *New Phytologist*, 225(1), 105–112. <https://doi.org/10.1111/nph.16055>
- Sperry, J. S., & Love, D. M. (2015). What plant hydraulics can tell us about responses to climate-change droughts. *New Phytologist*, 207(1), 14–27. <https://doi.org/10.1111/nph.13354>
- Sperry, J. S., Venturas, M. D., Anderegg, W. R. L., Mencuccini, M., Mackay, D. S., Wang, Y., & Love, D. M. (2017). Predicting stomatal responses to the environment from the optimization of photosynthetic gain and hydraulic cost. *Plant, Cell and Environment*, 40(6), 816–830. <https://doi.org/10.1111/pce.12852>
- Sperry, J. S., Venturas, M. D., Todd, H. N., Trugman, A. T., Anderegg, W. R. L., Wang, Y., & Tai, X. (2019). The impact of rising CO₂ and acclimation on the response of US forests to global warming. *Proceedings of the National Academy of Sciences*, 116(51), 25734–25744. <https://doi.org/10.1073/pnas.1913072116>
- Sperry, J. S., Wang, Y., Wolfe, B. T., Mackay, D. S., Anderegg, W. R. L., McDowell, N. G., & Pockman, W. T. (2016). Pragmatic hydraulic theory predicts stomatal responses to climatic water deficits. *New Phytologist*, 212(3), 577–589. <https://doi.org/10.1111/nph.14059>
- Sun, Y., Frankenberg, C., Jung, M., Joiner, J., Guanter, L., Köhler, P., & Magney, T. (2018). Overview of solar-induced chlorophyll fluorescence (SIF) from the orbiting carbon observatory-2: Retrieval, cross-mission comparison, and global monitoring for GPP. *Remote Sensing of Environment*, 209, 808–823. <https://doi.org/10.1016/j.rse.2018.02.016>
- Sun, Y., Frankenberg, C., Wood, J. D., Schimel, D., Jung, M., Guanter, L., et al. (2017). OCO-2 advances photosynthesis observation from space via solar-induced chlorophyll fluorescence. *Science*, 358(6360), eaam5747. <https://doi.org/10.1126/science.aam5747>
- Taylor, K. E., Stouffer, R. J., & Meehl, G. A. (2012). An overview of cmip5 and the experiment design. *Bulletin of the American Meteorological Society*, 93(4), 485–498. <https://doi.org/10.1175/bams-d-11-00094.1>
- Terrer, C., Jackson, R. B., Prentice, I. C., Keenan, T. F., Kaiser, C., Vicca, S., et al. (2019). Nitrogen and phosphorus constrain the CO₂ fertilization of global plant biomass. *Nature Climate Change*, 9(9), 684–689. <https://doi.org/10.1038/s41558-019-0545-2>
- Tramontana, G., Jung, M., Schwalm, C. R., Ichii, K., Camps-Valls, G., Ráduly, B., et al. (2016). Predicting carbon dioxide and energy fluxes across global fluxnet sites with regression algorithms. *Biogeosciences*, 13(14), 4291–4313. <https://doi.org/10.5194/bg-13-4291-2016>
- Trugman, A. T., Medvigy, D., Mankin, J. S., & Anderegg, W. R. L. (2018). Soil moisture stress as a major driver of carbon cycle uncertainty. *Geophysical Research Letters*, 45(13), 6495–6503. <https://doi.org/10.1029/2018gl078131>
- Tucker, C. J. (1979). Red and photographic infrared linear combinations for monitoring vegetation. *Remote Sensing of Environment*, 8(2), 127–150. [https://doi.org/10.1016/0034-4257\(79\)90013-0](https://doi.org/10.1016/0034-4257(79)90013-0)
- Turner, D. P., Ritts, W. D., Cohen, W. B., Gower, S. T., Running, S. W., Zhao, M., et al. (2006). Evaluation of MODIS NPP and GPP products across multiple biomes. *Remote Sensing of Environment*, 102(3–4), 282–292. <https://doi.org/10.1016/j.rse.2006.02.017>
- van der Tol, C., Berry, J., Campbell, P., & Rascher, U. (2014). Models of fluorescence and photosynthesis for interpreting measurements of solar-induced chlorophyll fluorescence. *Journal of Geophysical Research: Biogeosciences*, 119(12), 2312–2327. <https://doi.org/10.1002/2014jg002713>
- van der Tol, C., Verhoef, W., Timmermans, J., Verhoef, A., & Su, Z. (2009). An integrated model of soil-canopy spectral radiances, photosynthesis, fluorescence, temperature and energy balance. *Biogeosciences*, 6(12), 3109–3129. <https://doi.org/10.5194/bg-6-3109-2009>

- van Genuchten, M. T. (1980). A closed-form equation for predicting the hydraulic conductivity of unsaturated soils. *Soil Science Society of America Journal*, 44(5), 892–898. <https://doi.org/10.2136/sssaj1980.03615995004400050002x>
- Venturas, M. D., Sperry, J. S., Love, D. M., Frehner, E. H., Allred, M. G., Wang, Y., & Anderegg, W. R. L. (2018). A stomatal control model based on optimization of carbon gain versus hydraulic risk predicts aspen sapling responses to drought. *New Phytologist*, 220(3), 836–850. <https://doi.org/10.1111/nph.15333>
- Walker, A. P., Beckerman, A. P., Gu, L., Kattge, J., Cernusak, L. A., Domingues, T. F., et al. (2014). The relationship of leaf photosynthetic traits- V_{cmax} and J_{max} -to leaf nitrogen, leaf phosphorus, and specific leaf area: A meta-analysis and modeling study. *Ecology and Evolution*, 4(16), 3218–3235. <https://doi.org/10.1002/ece3.1173>
- Wang, Y. (2023a). Clima land code archive [Software]. Zenodo. <https://doi.org/10.5281/zenodo.7526252>
- Wang, Y. (2023b). Clima land global simulations archive [Dataset]. Zenodo. <https://doi.org/10.5281/zenodo.7526232>
- Wang, Y., & Frankenberg, C. (2022a). On the impact of canopy model complexity on simulated carbon, water, and solar-induced chlorophyll fluorescence fluxes. *Biogeosciences*, 19(1), 29–45. <https://doi.org/10.5194/bg-19-29-2022>
- Wang, Y., & Frankenberg, C. (2022b). Technical note: Common ambiguities in plant hydraulics. *Biogeosciences*, 19(19), 4705–4714. <https://doi.org/10.5194/bg-19-4705-2022>
- Wang, Y., Köhler, P., Braghieri, R. K., Longo, M., Doughty, R., Bloom, A. A., & Frankenberg, C. (2022). Griddingmachine, a database and software for earth system modeling at global and regional scales. *Scientific Data*, 9(1), 258. <https://doi.org/10.1038/s41597-022-01346-x>
- Wang, Y., Köhler, P., He, L., Doughty, R., Braghieri, R. K., Wood, J. D., & Frankenberg, C. (2021). Testing stomatal models at the stand level in deciduous angiosperm and evergreen gymnosperm forests using clima land (v0.1). *Geoscientific Model Development*, 14(11), 6741–6763. <https://doi.org/10.5194/gmd-14-6741-2021>
- Wang, Y., Sperry, J. S., Anderegg, W. R. L., Venturas, M. D., & Trugman, A. T. (2020). A theoretical and empirical assessment of stomatal optimization modeling. *New Phytologist*, 227(2), 311–325. <https://doi.org/10.1111/nph.16572>
- Wang, Y. P., Baldocchi, D., Leuning, R., Falge, E., & Vesala, T. (2007). Estimating parameters in a land-surface model by applying nonlinear inversion to eddy covariance flux measurements from eight fluxnet sites. *Global Change Biology*, 13(3), 652–670. <https://doi.org/10.1111/j.1365-2486.2006.01225.x>
- Wehr, R., Munger, J., McManus, J., Nelson, D., Zahniser, M., Davidson, E., et al. (2016). Seasonality of temperate forest photosynthesis and daytime respiration. *Nature*, 534(7609), 680–683. <https://doi.org/10.1038/nature17966>
- Wei, Y., Liu, S., Huntzinger, D. N., Michalak, A. M., Viovy, N., Post, W. M., et al. (2014). The North American carbon program multi-scale synthesis and terrestrial model intercomparison project—Part 2: Environmental driver data. *Geoscientific Model Development*, 7(6), 2875–2893. <https://doi.org/10.5194/gmd-7-2875-2014>
- Wu, G., Guan, K., Jiang, C., Peng, B., Kimm, H., Chen, M., et al. (2020). Radiance-based NIRv as a proxy for GPP of corn and soybean. *Environmental Research Letters*, 15(3), 034009. <https://doi.org/10.1088/1748-9326/ab65cc>
- Yang, P., Verhoef, W., & van der Tol, C. (2017). The mSCOPE model: A simple adaptation to the scope model to describe reflectance, fluorescence and photosynthesis of vertically heterogeneous canopies. *Remote Sensing of Environment*, 201, 1–11. <https://doi.org/10.1016/j.rse.2017.08.029>
- Yuan, H., Dai, Y., Xiao, Z., Ji, D., & Shangguan, W. (2011). Reprocessing the modis leaf area index products for land surface and climate modeling. *Remote Sensing of Environment*, 115(5), 1171–1187. <https://doi.org/10.1016/j.rse.2011.01.001>
- Zhang, Y., Guanter, L., Berry, J. A., van der Tol, C., Yang, X., Tang, J., & Zhang, F. (2016). Model-based analysis of the relationship between sun-induced chlorophyll fluorescence and gross primary production for remote sensing applications. *Remote Sensing of Environment*, 187, 145–155. <https://doi.org/10.1016/j.rse.2016.10.016>
- Zhang, Y., Xiao, X., Wu, X., Zhou, S., Zhang, G., Qin, Y., & Dong, J. (2017). A global moderate resolution dataset of gross primary production of vegetation for 2000–2016. *Scientific Data*, 4(1), 170165. <https://doi.org/10.1038/sdata.2017.165>
- Zhang, Y., & Ye, A. (2021). Would the obtainable gross primary productivity (GPP) products stand up? A critical assessment of 45 global GPP products. *Science of the Total Environment*, 783, 146965. <https://doi.org/10.1016/j.scitotenv.2021.146965>

References From the Supporting Information

- Jiang, C., & Fang, H. (2019). GSV: A general model for hyperspectral soil reflectance simulation. *International Journal of Applied Earth Observation and Geoinformation*, 83, 101932. <https://doi.org/10.1016/j.jag.2019.101932>